DOE/NASA/0282-1
NASA CR-185174
R89-917447-32

Identification of a Cast Iron Alloy Containing Nonstrategic Elements

Final Report

C.V. Cooper, D.L. Anton, F.D. Lemkey, H. Nowotny, R.S. Bailey,
L.H. Favrow, J.G. Smeggil, and D.B. Snow
United Technologies Research Center

June 1989

Prepared for
NATIONAL AERONAUTICS AND SPACE ADMINISTRATION
Lewis Research Center
Under Contract DEN3-282

for
U.S. DEPARTMENT OF ENERGY
Conservation and Renewable Energy
Office of Vehicle and Engine R&D

DISCLAIMER

Printed in the United States of America

Available from
National Technical Information Service
U.S. Department of Commerce
5285 Port Royal Road
Springfield, VA 22161

NTIS price codes[1]
Printed copy: A05
Microfiche copy: A01

[1]Codes are used for pricing all publications. The code is determined by the number of pages in the publication. Information pertaining to the pricing codes can be found in the current issues of the following publications, which are generally available in most libraries: *Energy Research Abstracts (ERA); Government Reports Announcements* and Index (*GRA* and I); *Scientific and Technical Abstract Reports (STAR);* and publication, NTIS-PR-360 available from NTIS at the above address.

DOE/NASA/0282-1
NASA CR-185174
R89-917447-32

Identification of a Cast Iron Alloy Containing Nonstrategic Elements

Final Report

C.V. Cooper, D.L. Anton, F.D. Lemkey, H. Nowotny, R.S. Bailey,
L.H. Favrow, J.G. Smeggil, and D.B. Snow
United Technologies Research Center
East Hartford, Connecticut 06108

June 1989

Prepared for
National Aeronautics and Space Administration
Lewis Research Center
Cleveland, Ohio 44135
Under Contract DEN3-282

for
U.S. DEPARTMENT OF ENERGY
Conservation and Renewable Energy
Office of Vehicle and Engine R&D
Washington, D.C. 20545
Under Interagency Agreement DE-AI01-77CS51040

CONTENTS

1.0 EXECUTIVE SUMMARY

A program has been carried out to address the mechanical and environmental needs of Stirling engine heater head and regenerator housing components, while reducing the dependence on strategic materials. Current candidate materials for such applications contain significant levels of cobalt, nickel, chromium, and/or tantalum. An alloy was developed during this program which contained none of these strategic elemental additions *per se*. The base is iron with additions of manganese, molybdenum, carbon, silicon, niobium, and ferro–chromium. Such an alloy should be producible on a large scale at very low cost.

The resulting alloy, designated as NASAUT 4G–A1, contained 15 Mn, 15Cr, 2 Mo, 1.5 C, 1.0 Si, 1.0 Nb (in weight percent) with a balance of Fe. This alloy (and several others along the development path) was optimized for chemistry, based upon tensile strength, creep–rupture strength, fracture behavior, and fatigue resistance up to 800°C. Alloys were also tested for environmental compatibility (in air, salt fog, and hydrogen). The microstructure and mechanical properties (including hardness) were assessed in the as–cast condition and following several heat treatments, including one designed to simulate a required braze cycle. The alloy was fabricated and characterized in the form of both equiaxed and columnar–grained castings. The columnar grains were produced by directional solidification, and the properties were characterized in both the longitudinal and transverse orientations.

The NASAUT 4G–A1 alloy was found to be good in cyclic–oxidation resistance and excellent in both hydrogen and hot–corrosion resistance, especially in comparison to the baseline XF–818 alloy. The mechanical properties of yield strength, stress–rupture life, high–cycle–fatigue resistance, and low–cycle–fatigue resistance were good to excellent in comparison to the current alloy for this application, HS–31 (X–40), with precise results depending in a complex manner on grain orientation and temperature. If required, the ductility could be improved by lowering the carbon content.

In summary, a castable, low–cost, iron–based superalloy has been demonstrated with excellent stress–rupture properties and environmental resistance in oxygen and hydrogen to 800°C. This alloy may be appropriate for automotive Stirling engine as well as other applications requiring low–cost, heat–resisting alloys.

2.0 INTRODUCTION

A need exists for a low–cost, cast, iron–based alloy which can be used for improved automotive Stirling engine cylinder and regenerator housing components. This alloy must meet the requirements of high strength and thermal–fatigue resistance to 800°C, must be compatible with and have low permeability to hydrogen, must possess elevated temperature oxidation/corrosion resistance, and must contain a minimum of strategic elements. Alloys in prototype automotive Stirling engines under Department of Energy (DOE) development programs (Ref. 1) have not met all of these criteria, particularly with regard to alloy cost and availability. The purpose of this program has been to address the development of a cast, iron–based alloy, utilizing alloying additions such as manganese, aluminum, carbon, and nitrogen, such that a shift away from additions such as cobalt and nickel is rendered

possible. Because of the higher carbon levels of the alloys developed as part of this program (> 1.0 wt %), ferro-chromium, derived from chromite deposits found in the western United States, has become a viable source for chromium additions. Until recently, these chromite deposits had been considered too low grade for stainless steel manufacturers because of the lower chromium-to-iron ratio of 1.5:1 and their higher carbon content (Ref. 2).

This program has consisted of an initial alloy-composition iteration and properties determination phase, in which results of cyclic-oxidation, tensile, and stress-rupture tests were used to screen alloys. The base alloy composition originated from the austenitic matrix of a directionally solidified (DS) eutectic composite which was originally developed for aircraft gas turbine use (Ref. 3). Following the determination of an initial alloy composition, based on a balance of physical and mechanical properties, extensive studies were focused on the variation of tensile fatigue properties with temperature. Investment-cast test bars were produced and given various heat treatments to optimize properties and to simulate possible brazing cycles. In addition, extensive microstructural investigations were conducted to characterize the as-cast and heat-treated microstructures.

Another objective of this study was to determine the possibility of increasing the ductility and improving the high- and low-cycle-fatigue properties of the alloy without sacrificing strength by modifications in the carbon content. This was followed by a study to determine the degree of anisotropy in the directionally solidified (DS) castings by examining the mechanical properties of simulated-braze-cycled (SBC), longitudinally and transversely oriented specimens.

This study has produced a high-carbon, castable, iron-based superalloy with excellent stress-rupture and oxidation properties. The final alloy, designated NASAUT 4G-A1, has been shown to remain virtually unaffected by high temperature hydrogen exposure at standard pressure. The maximum temperature for use of this alloy is 800°C (1472°F), far in excess of conventional stainless steels. Most importantly, this alloy has been found to have a raw-materials cost of $0.37/kg ($0.81/lb) (Refs. 4 and 5) by containing nonstrategic materials, only.

3.0 RESULTS AND DISCUSSION

3.1 Alloy Design

The initial eutectic-alloy composition of 10 Cr, 20 Mn, 3.3 C, bal Fe (all compositions given in wt % unless otherwise specified) (Ref. 3) was modified by removing carbon in order to obtain a castable, austenitic alloy. Thus, the original alloy composition, designated as NASAUT 1, contained 10 Cr, 20 Mn, 1.5 C, bal Fe. The iteration flow chart used for alloy modifications to enhance stress-rupture and oxidation resistance is given in Fig. 1.

The first alloy iteration included modifying the Cr and Mn compositions to 15 ± 5, Mo to 10, C at 1.0 and 1.5, and Al to 2. These alloys were obtained by induction melting commercial purity starting elements and pouring into Cu-molded chill bars. Subsequent vacuum re-melting and solidification through a 200°C/cm thermal gradient at 10 cm/h were used to eliminate shrinkage pipe and produce sound test specimens.

A major emphasis of this program was the x-ray identification of phases within the alloys as a function of constituent concentration. The degree of matrix stability as well as the carbide types and volume fractions were monitored. The base alloy, NASAUT 1, maintained an austenitic, FCC matrix which contained 12 vol % carbides, primarily of the M_7C_3-type.

Tensile tests were carried out at ambient temperature and 788°C (1450°F) in air at a strain rate of 0.01 min^{-1}. To summarize the initial program results, an increase in the carbon content was found to increase the strength significantly and decrease the ductility of the alloys; minor Mo additions were found to be beneficial to strength.

Two alloys were clearly superior in stress-rupture performance at 776°C at stresses between 170 and 240 MPa in air. The base alloy and that designated NASAUT 4, having the composition 15 Mn, 12 Cr, 3 Mo, 1.5 C, and bal Fe, maintained superior stress-rupture lives compared to the other candidate alloys.

Cyclic-oxidation tests were conducted by heating round, penny-shaped specimens in air to 871°C for 55 min and withdrawing to ambient temperature for 5 min. Based on mass changes per unit surface area, NASAUT alloys #1, #3, and #4 maintained the greatest resistance to surface attack. Aluminum additions were found to increase the surface stability and elevated-temperature ductility of these alloys greatly; however, these additions were found to be quite deleterious to the stress-rupture and tensile strength.

From the above results, NASAUT alloys #1 and #4 were promoted to the second alloying iteration based on the combination of improved tensile strengths, superior rupture lives, and good oxidation resistance.

A second alloy iteration was performed on the above two mentioned compositions. In this case, Al was varied from 0 to 5, Si from 0 to 1.5, Nb from 0 to 1.0, and Mo from 0 to 3.0. Screening again on stress-rupture and tensile strength, two alloys, 1G and 4G, were observed to have superior attributes. Alloy 4G was found to have greater room-temperature tensile strength than 1G, while their elevated temperature properties were similar. The compositions were 10 Mn, 20 Cr, 1.5 C, 1.0 Si, and bal Fe and 15 Mn, 12 Cr, 3 Mo, 1.5 C, 1.0 Si, 1.0 Nb, and bal Fe for alloys 1G and 4G, respectively. Aluminum additions were discontinued due to the deleterious effects on stress-rupture properties. Silicon was found to have the same beneficial effects in terms of cyclic-oxidation resistance; therefore, it has become an important alloy constituent. The niobium was found to precipitate the primary NbC, which helped to strengthen the 4G alloy; furthermore, its role in promoting improved sulfidation resistance was found to be critical. On the basis of its superior ambient-temperature strength, NASAUT 4G was selected for further alloy modification.

In the third alloy iteration, the following modifications were made to 4G: Cr ± 3, Mo -1, Nb -0.5, Si +2, and B +0.1. Chromium was added to increase rupture life, silicon was added to enhance oxidation resistance, and boron was added to precipitate the M_3B_2 phase and enhance strength.

Stress-rupture testing was conducted on specimens aged at 650°C for 100 h to simulate operating exposure. The boron additions resulted in a small debit to rupture life and was, therefore,

discontinued. Chromium additions enhanced stress-rupture behavior, while reductions in the refractory metals were deleterious to the rupture life. Further additions of silicon (> 1%) failed to enhance the oxidation resistance of the alloy and were deemed unnecessary. This led to the selection of alloy 4G-A, containing 15 Mn, 15 Cr, 2 Mo, 1.5 C, 1.0 Si, 1.5 Nb, and bal Fe.

The final alloy iteration included rare-earth additions to the alloy and a further attempt to reduce the refractory content. Only the addition of 0.5 yttrium was found to be beneficial to cyclic-oxidation resistance, while the other rare-earth elements produced no significant effect other than a slight debit to oxidation resistance. A slight reduction in the niobium content to 1.0 was found to have little effect on rupture life and was found to promote cyclic-sulfidation resistance (Ref. 6). The contribution from yttrium was deemed insufficient to include it as an alloy constituent. Thus, the final alloy chemistry devised here was given the designation NASAUT 4G-A1 and contained 15 Mn, 15 Cr, 2 Mo, 1.5 C, 1.0 Si, 1.0 Nb, and bal Fe. In this alloying scheme, NASAUT 4G-A1 was determined to have the best combination of tensile and stress-rupture strength and cyclic-oxidation and -sulfidation stability. The stress-rupture data for this alloy are given in Fig. 2, where several other candidate alloys for Stirling engine heater head assemblies are compared to the final alloy iteration of this study. The cyclic-oxidation results for NASAUT 4G-A1, a number of 4G-alloy modifications, and the alloys HS-31 and XF-818 are shown in Fig. 3.

3.2 Hydrogen Exposure

To determine the stability of this alloy to hydrogen, a specimen was creep tested in 101 kPa (1 atm) of dynamic H_2 at 900°C after an initial heat treatment of 650°C/100 h in air. No significant loss in rupture life was observed from the tests conducted in flowing hydrogen. In addition, no H_2 pick-up was evident upon microstructural or chemical analyses. The carbide network showed no signs of reduction, even at the specimen surface, illustrating its resistance to hydrogen attack at temperatures less than or equal to 900°C.

3.3 Corrosion Resistance

As discussed above, a test of the corrosion resistance of HS-31, XF-818, and NASAUT 4G-A1 was made by exposing these alloys at 871°C to 35ppm NaCl aspirated in air, typical of the environment adjacent to the ocean or on a street spread with salt to remove ice. The results were quite dramatic, as shown in Fig. 4. It is clear that both HS-31 and NASAUT 4G-A1 were resistant to salt corrosion, while the XF-818 coupon was completely consumed.

3.4 Low-Cycle-Fatigue Behavior

Constant-strain-amplitude, low-cycle-fatigue tests were conducted at 800°C in air on specimens produced as described previously. Throughout this program, low-cycle-fatigue tests were conducted in laboratory air under total-strain control. A constant total strain rate of 0.005 sec^{-1} was maintained through the application of a completely reversed ($R' = -1$), triangular waveform. The results of these tests are given in Fig. 5, where comparison is made to HS-31, a cobalt-based alloy used in experimental automotive Stirling engine designs because of its resistance to hydrogen attack. The

results indicate that NASAUT 4G-A1 is a factor of 5 to 10 superior to HS-31 in terms of LCF performance. This is especially apparent at low strain amplitudes, where run-out was experienced at a significantly higher strain amplitude for alloy 4G-A1.

Subsequent analysis of the fatigue data indicated that the measured modulus for the specimens was significantly lower than that expected for polycrystalline austenitic iron. The lower modulus is believed to have resulted from the DS process utilized. This process achieved essentially a pore-free alloy (neglecting microporosity) with a columnar, dendritic structure, having predominantly a [001] texture aligned with the growth axis. Subsequent screening-type mechanical tests were carried out on finer-sized, equiaxed-grain castings.

3.5 As-Cast Microstructure

A typical optical micrograph of alloy NASAUT 4G-A1 after LCF testing for 12 hours at 800°C is given in Fig. 6. Here feature "A" has been identified as the primary NbC, feature "B" as the Cr-rich Cr_7C_3, and feature "C" as a two-phase precipitate with "a" being a manganese-sulfide inclusion and "b" being a manganese-aluminum-sulfide inclusion. The latter exhibits quite an innocuous form and is considered to be an excellent means of desulfurizing the alloy. Both of the carbides are considered to help in strengthening the alloy.

3.6 Heat-Treatment Optimization and Microstructure

The age-hardening response of this alloy has been investigated in an attempt to optimize the heat treatment. An isothermal aging curve is given in Fig. 7. Classical aging is demonstrated, with continuous hardening being displayed through 100 h at temperatures below 760°C; however, hardening followed by softening is exhibited at higher temperatures. This behavior is indicative of the coarsening of fine precipitates.

To verify the hardening response, a TEM investigation was conducted on specimens aged at 870°C/8 h, an under age, and 980°C/32 h, an over age. Representative microstructures for these two heat treatments are presented in Figs. 8 and 9. The small, cuboidal plates are $M_{23}C_6$ precipitates, which were identified previously via x-ray analysis; the grid pattern of faults was identified as stacking faults forming on (111) planes. Faults exhibiting similar morphology have been reported to be precursors to $M_{23}C_6$ precipitates (Ref. 7). This is consistent with the plate-like morphology of the $M_{23}C_6$ precipitates shown in Fig. 8. As displayed in Fig. 9, overaging has minimized the occurrence of faults, leaving behind the coarse $M_{23}C_6$.

3.7 Equiaxed-Cast Properties

Since the tensile and low-cycle-fatigue properties were observed to depend acutely on the modulus of the material, equiaxed-cast bars were prepared and specimens machined in order to duplicate the LCF results reported above. Shell-mold castings of NASAUT 4G-A1 were produced by Garrett AiResearch Co. Metallographic examination revealed the microstructure to consist of equiaxed grains having interdendritic spacings of between 20 and 40 μm (Fig. 18).

3.7.1 Heat-Treatment Optimization. In addition to the as-cast properties, three heat treatments were devised to study the influence of heat treatment on properties. As partially described above, these heat treatments were: (a) 760°C/8 h, designated as "under aged," (b) 760°C/20 h + 870°C/10 h, designated as "super aged," which produced the highest R_c hardness measured in this alloy, and (c) 1065 C/30 min + 790°C/16 h + 650°C/16 h, designated as the "simulated-braze cycle" (SBC), which is a variation on the Mod II standard braze cycle which MTI uses during the manufacture of automotive Stirling engine heater heads (Ref. 8).

3.7.2 Tensile Properties. The results of the tensile tests on these four heat-treated alloys are given graphically in Fig. 10 and 11 and tabularly in Table I, where yield strength and strain-to-failure are plotted as a function of temperature through 900°C. The super-aged alloy maintains superior strength through 600°C compared to the other heat-treated specimens. Above this temperature, all of the alloys converge to approximately the same strength. The strain-to-failure is inversely related to the strength of the alloy, with the as-cast heat treatment maintaining approximately 4% strain-to-failure and the other specimens failing after 1 to 2% strain. Above 600°C, the strain-to-failure of all alloys increases dramatically. These data, when compared to those of alloy XF-818 in Fig. 12, show the superior low- and intermediate-temperature strength of equiaxed alloy NASAUT 4G-A1. At elevated temperatures, the strength of the two alloys is comparable, while the ductility of 4G-A1 is superior at all temperatures.

3.7.3 Low-Cycle-Fatigue Behavior. Low-cycle-fatigue tests were conducted on the equiaxed specimens in the as-cast condition in a fashion similar to that described previously. These results are given graphically in Fig. 13 along with the DS data and XF-818 data presented in Fig. 5; the data are presented tabularly in Tables II and III. The equiaxed-grain material produced substantially reduced fatigue lives compared to the original DS form but maintained a slight advantage over the XF-818 alloy.

3.7.4 Low-Cycle-Fatigue Behavior for Simulated-Braze-Cycled (SBC) Condition. The braze processing used to integrate certain automotive Stirling engine heater head components rendered the determination of the LCF properties in the simulated-braze-cycled (SBC) condition increasingly important. A comparison of the LCF behavior at 800°C for the SBC and as-cast conditions is given in Figs. 14 and 15 (*cf.* Tables II and III). As shown, the simulated-braze cycle proved to be detrimental at the lower strain amplitudes at 800°C, only. At a constant strain amplitude of ±0.4%, the SBC treatment resulted in inferior lives when compared to the as-cast condition at temperatures below 600°C. Further subsequent characterization of the LCF behavior in the SBC condition at temperatures of 22°C and 800°C has been presented in Fig. 16.

3.7.5 High-Cycle-Fatigue Behavior. High-cycle-fatigue tests were conducted on SBC, equiaxed-cast specimens at a temperature of 800°C. For this, a sinusoidal waveform at a frequency of 20 Hz was employed at an R-ratio of 0.1. The results from these tests have been summarized graphically in Fig. 16 and tabularly in Table IV. These results have been produced to satisfy the concern that, in addition to low-cycle fatigue, high-cycle fatigue has been an active failure mode within the heater head and other components of the automotive Stirling engine. These results are to be compared to the HCF performance of the transversely and longitudinally oriented DS material in the SBC condition, as described below.

3.8 Carbon Modification

A final alloy iteration was performed to determine the possibility of increasing the strain-to-failure of the alloy without sacrificing strength. To do this, three additional alloys were prepared in equiaxed form, having chemistries identical to that of NASAUT 4G-A1, with the modification that each had successively a 0.25% decrement in carbon content. Thus, alloys 4G-A2, 4G-A3, and 4G-A4 had 1.25, 1.00, and 0.75% C, respectively. Optical microscopic examinations revealed substantial modifications to the interdendritic carbides, as shown in Figs. 18 and 19.

3.8.1 Mechanical Properties Evaluation. The results of tensile tests on the carbon-modified alloys in the SBC condition are summarized graphically in Fig. 20 and tabularly in Table V. In Fig. 20, both the 0.2% offset yield stress and strain-to-failure are plotted as a function of carbon concentration at 600°C. The yield strength decreases linearly with decreasing carbon content from 350 to 250 MPa (a 30% decrease), while the strain-to-failure increases from 1 to 10% (a 1000% increase). Tests at other temperatures yield similar results. While these results demonstrate that high-ductility alloys are derivable through carbon modification, it may be cost ineffective to alter the composition of the alloy. The effects of the carbon reduction on low-cycle-fatigue performance of equiaxed-cast 4G-A alloys are summarized in Fig. 21 and Table VI. While there is significant scatter in the results, it is generally true that the LCF performance varies inversely with carbon content at 800°C.

3.9 Properties of Transversely Oriented, Directionally Solidified (Columnar Grain) Castings in the SBC Condition

To determine the suitability of using directional solidification to produce automotive Stirling engine heater head components, the properties of directionally solidified castings in the SBC were investigated. During the initial phase of this program modification, significant problems were encountered in achieving castings with the proper chemistry. Initial DS casting attempts utilizing an atmosphere of argon at a pressure of 60 Pa (0.45 torr) resulted in a significant deficit in Mn, due to its volatility at the pouring temperature of 1500°C. Ultimately, successful chemical compositions were achieved by reducing the pouring temperature to 1468°C, increasing the argon pressure to approximately 50 kPa (380 torr), using less reactive crucibles of MgO, and utilizing crucible and mold covers to minimize volatile losses. These changes and a DS casting rate of 25 cm/h were used successfully to produce all slab castings.

The macrograph of a typical, macroetched DS slab from which specimens were machined is presented in Fig. 22. The result of the directional solidification was a columnar-grained structure sharing a common (001) zone axis, which was within 10° of being parallel to the DS axis. Transverse sectioning of the DS slabs indicated that they were sound castings with little or no pipe porosity, which rendered them suitable for machining into test specimens. The as-cast microstructure for the DS form contained both primary, Nb-rich MC carbides, which exhibited a script appearance, and blocky, Cr- and Mn-rich M_7C_3 carbides. The representative microstructure for a longitudinal section is presented in Fig. 23.

3.9.1 Tensile Properties. Initially, the focus was placed on a determination of properties for specimens in which the stress or strain axis was transverse to the DS direction (DS/T). A constant total strain rate of 0.05 min^{-1} was employed for all monotonic tensile tests unless otherwise noted.

The tensile properties of the transversely oriented DS material in the SBC condition are summarized in Table VIII. Graphical representations of the DS/T tensile yield and strain-to-failure properties are presented in Figs. 24 and 25. A comparison to the equiaxed-cast material, Figs. 10 and 11, reveals the superiority in the strain-to-failure of the DS/T form throughout the temperature range investigated. Furthermore, the DS/T form exhibits higher Young's moduli essentially throughout the temperature range investigated. However, the equiaxed-cast form is clearly superior to the DS/T form in terms of the 0.2% offset yield stress and ultimate tensile stress (not shown), particularly at temperatures between 22 and 400°C.

3.9.2 Fracture Behavior at 22°C. Some very interesting and unexpected results have been obtained from an investigation into the fracture behavior of transversely and longitudinally oriented NASAUT 4G-A1 in the SBC condition. Initial problems in precracking the brittle alloy at room temperature were overcome by cycling at a stress intensity which was only slightly greater than the ultimate K_{IC} as determined from the quasi-static fracture of the fatigue-precracked, compact tension specimens. A schematic diagram illustrating the two orientations investigated is given in Fig. 26. Interestingly and unexpectedly, the transverse (T-L) orientation, in which the crack plane lay parallel to the DS axis, exhibited a plane-strain fracture toughness which was more than twice the value in the longitudinal (L-T) orientation, 23.0 $MPa \bullet m^{1/2}$ and 10.0 $MPa \bullet m^{1/2}$, respectively, as summarized in Table IX. For the former, gross examination of the fracture surfaces revealed a less-planar fracture path which appeared to follow the dendrite cores.

In contrast, the fracture surface of the L-T orientation was quite flat and the dendrite cores were fractured without much energy absorption. The resulting surface resembled what has been termed a "fossil record" morphology, with occasional dendrite cores having been extracted from the alloy matrix. Low-magnification fractographs of the two orientations are shown in Fig. 27. As shown clearly in Fig. 28, ductile tearing through the dendrite cores and cleavage across the interdendritic carbide network were the active failure mechanisms for the T-L orientation. In addition to the dendrite core identified as "A" and positioned on the left side of Fig. 28a, a secondary dendrite arm from an adjacent dendrite (feature "B") fractured in a ductile manner, as well.

Additional SEM was devoted to the resolution of the mechanism which led to the toughening of the alloy in the T-L orientation by sectioning the fractured specimens as shown schematically in Fig. 29. Examination of Fig. 30 for the L-T orientation reveals that the fracture path was directly through the interdendritic carbide network, between the secondary dendrite arms. Limited secondary cracking is clear from this micrograph, also. Secondary cracking was much more prevalent in the T-L orientation, however, as shown in Fig. 31. The creation of this additional crack surface area in the bifurcated, secondary cracks has required additional energy input, the result of which was higher toughness for the T-L orientation.

3.9.3 Low-Cycle-Fatigue Behavior. In a similar manner to the procedures and results presented earlier for the equiaxed-cast form, the low-cycle-fatigue behavior of the SBC, DS/T form of NASAUT 4G-A1 has been characterized at the single temperature of 800°C. The results from these tests have been summarized graphically in Fig. 32 and tabularly in Table X. While a linear fit to the data may be forced as shown by the solid line, the dashed line, which represents a least-squares fit to a quadratic equation, improves the quality of the fit. Deviations from linearity for fully logarithmic

graphs of strain–life data, the so–called Coffin–Manson relationship (Refs. 9 and 10), are not isolated. For example, Cooper and Fine (Ref. 11) ascribed deviations from linearity in the endurance behavior of vacuum–melted α–iron to the operation of two independent processes, those of microcrack initiation and propagation, among others. Clearly, the mechanisms which operate actively during these independent processes vary.

Also bothersome in Fig. 32 is the greater scatter in the lifetimes–to–failure compared to the equiaxed–cast behavior (*cf.* Fig. 13). The comparatively greater degree of scatter may be ascribable, in part, to the brittle fracture paths which have been observed to operate during quasi–static fracture, as documented above.

3.9.4 High–Cycle–Fatigue Behavior. HCF tests have been conducted on the SBC, DS/T 4G–A1 alloy in a similar manner to that reported above for the equiaxed–cast material. A sinusoidal waveform utilizing a cyclic frequency 20 Hz and an R–ratio of 0.1 has been used throughout the HCF testing. The range of temperatures investigated has been from 22°C to 800°C, inclusive. The results are summarized graphically in Figs. 17 and 33–36 and tabularly in Tables XI through XVI. While the DS/T form seems to exhibit parity or superiority at the two lower temperatures of 22°C and 200°C, this trend reverses quickly for tests conducted at the intermediate temperature of 400°C, as shown in Fig. 35. Parity in HCF lives is reestablished at 600°C and is retained at 800°C, as shown in Figs. 36 and 17. For convenience in comparing the results, HCF data for the equiaxed–cast form have been superimposed onto the graphs for the DS/T form. As noted for the results from the LCF testing of the DS/T form, a disturbingly high degree of scatter is evident for the HCF results. In general, the degree of scatter has been observed to increase with increasing temperature.

Attempts to understand this scatter by applying SEM to the fracture surfaces were essentially unsuccessful. Similarly, attempts to understand the scatter according to the variation in columnar grain and carbide sizes as a consequence of the specimen position within the slab casting, proved inconclusive.

3.10 Properties of Longitudinally Oriented, Directionally Solidified (Columnar Grain) Castings in the SBC Condition

3.10.1 Creep Behavior. The characterization of the creep behavior of SBC, DS/L 4G–A1 was investigated at the single temperature of 800°C. The objective was to determine whether the longitudinal orientation would satisfy the design requirement of achieving a creep strain of not greater than 2% in 500 h at the design stress of 120 MPa. The results of this creep testing are presented in Table XVII. Clearly, the longitudinal orientation of DS 4G–A1 is not capable of sustaining this severity of creep loading, rupturing in an average of 16.4 h under these design conditions. In order to determine a lower limit on the stress which would result in a maximum of 2% strain in 500 h at 800°C, the stress was lowered to 50 MPa, which sustained the 500 h exposure without having achieved a creep strain of even 1%. At the creep stress of 86 MPa, the average time to the achievement of 2% creep strain was 42.5 h.

3.10.2 Low–Cycle–Fatigue Behavior. The low–cycle–fatigue behavior of SBC, DS/L 4G–A1 has been investigated at the temperatures of 22°C, 400°C, and 800°C. The results from these tests are presented graphically in Figs. 37–39 and tabularly in Table XVIII. While the equiaxed–cast form is

clearly superior at 22°C, parity between the two forms is achieved quickly for the two higher temperatures of 400°C and 800°C. Again evident from Fig. 39 is the nonlinearity between strain amplitude and cycles-to-failure as graphed in fully logarithmic coordinates.

3.10.3 High-Cycle-Fatigue Behavior. The high-cycle-fatigue behavior of the SBC, DS/L form has been investigated at the temperatures of 22°C, 400°C, and 800°C. The results from these tests are presented graphically in Figs. 40–42 and tabularly in Table XIX. As for the DS/T form reported above, the HCF results for the DS/L form exhibit a high degree of scatter. This scatter is particularly prevalent at the temperatures of 22°C and 400°C, while being somewhat reduced for the data at 800°C. Comparison to the equiaxed-cast form reveals that the HCF performance of the DS/L form is inferior, with the possible exception being at the temperature of 800°C, where the lifetimes-to-failure are similar.

3.10.4 Tensile Properties. The tensile properties for NASAUT 4G-A1 in the SBC, DS/L condition are presented in Table XX. It should be noted that the strain rate was inconsistent over the range of temperatures investigated due to vendor error, being 0.05 min^{-1} for the tests conducted at 22 and 400°C and 0.005 min^{-1} for the tests conducted at 200, 600, and 800°C. This error may cause difficulty in drawing exact comparisons in the 0.2% offset and ultimate tensile stresses among the DS/L, DS/T, and equiaxed forms due to the moderate strain-rate sensitivity of austenitic alloys at elevated temperatures; however, it is expected to have a negligible effect on the strain-to-failure values. As expected, the elastic moduli are consistently lower for the DS/L form compared to both the equiaxed and DS/T forms, due to the (001) tensile orientation of the DS/L form. While the 0.2% offset yield and ultimate tensile stresses are comparable for the two orientations of the DS form in the SBC condition throughout the temperature range investigated, the ductility as measured by strain-to-failure is approximately equal at the two lower temperatures but is greatly superior for the DS/L compared to both the DS/T and equiaxed forms (in SBC condition) at higher temperatures, especially at 800°C (*cf.* Tables I, VIII, and XX).

4.0 SUMMARIZING REMARKS AND CONCLUSIONS

The completion of this program has resulted in the development of a cast, iron-based superalloy which may be processed in either conventional, equiaxed form or by directional solidification, in which case the (001) zone axis lies parallel or nearly parallel to the DS axis. While the alloy is high in chromium, it is not considered strategic because it does not rely on foreign supplies; rather, because of the high carbon content of the final alloy developed, 1.5%, the ferro-chromium deposits indigenous to the western U.S. are rendered viable sources. For the equiaxed form, the as-cast condition exhibits slightly inferior tensile strength but slightly superior ductility compared to the SBC condition. Similarly, the two additional heat treatments, the under-aged and super-aged conditions, display significantly superior strengths but fail to exhibit the monotonic strain tolerance of the as-cast condition. The low-cycle-fatigue performance in the as-cast condition is greatly superior to that in the SBC condition for temperatures less than 600°C, above which point the performance of the two conditions is approximately equal. For the HCF behavior, limited data indicate that the SBC condition is superior to the as-cast condition except at the extreme temperatures of 22°C and 800°C. In comparison to XF-818, the mechanical properties of equiaxed-cast NASAUT 4G-A1 are

equivalent or slightly superior; the greatest and most dramatic superiority of the latter is its resistance to oxidation, corrosion, and sulfidation. Decreasing the carbon content of the alloy from 1.5 to 0.75% produces an increase in the strain-to-failure and a concomitant decrease in tensile strength. The LCF performance varies approximately inversely with carbon content.

By comparison to the equiaxed-cast form of NASAUT 4G-A1, the transversely oriented DS form in the SBC condition is slightly to considerably weaker in monotonic tension and approximately equal in strain-to-failure throughout the temperature range investigated. The HCF behavior of the SBC, DS/T form is somewhat inferior to the equiaxed form at the lower temperatures but approaches parity at temperatures of 600°C and 800°C. Significant scatter in the HCF data is an increasing problem at the higher temperatures of 400 through 800°C.

Interestingly and surprisingly, the fracture toughness of the DS form in the transverse (T-L) orientation is approximately two times superior to that in the longitudinal (L-T) orientation. The reasons for this superiority are that the fracture surface follows the tougher dendrite cores and that the cracks tend to bifurcate in the T-L orientation; conversely, the fracture surface for the T-L orientation is rather flat and cleaves across the interdendritic carbide network.

ACKNOWLEDGEMENTS

The authors wish to acknowledge fruitful discussions and interactions with M. J. Cronin and J. A. Corey of Mechanical Technologies, Inc., Latham, NY. R. J. Henricks, A. S. Grot, and K. E. Taylor from the experimental foundry at Pratt & Whitney Division of United Technologies Corporation are gratefully acknowledged for their cooperation and efforts to produce the DS slab castings, from which properties in the simulated-braze-cycled (SBC) condition were determined. The able leadership of the technical program monitors, C. M. Scheuermann and R. H. Titran of NASA/Lewis Research Center, is acknowledged with appreciation.

5.0 REFERENCES

1. D. J. Schmatz and V. F. Zackay, Trans. ASM, 51, 299, 1959.

2. J. B. See, J. Met., 32 (4), 52, April 1980.

3. F. D. Lemkey, E. R. Thompson, J. C. Schuster, and H. Nowotny, in *In Situ Composites IV*, F. D. Lemkey, H. E. Cline, and M. McLean, eds., Elsevier Science Publising Co., Inc., New York, 1982, p. 31.

4. Metals Week, Nov. 23, 1984.

5. American Metal Market/Metal Working News, Nov. 19, 1984.

6. F. D. Lemkey, J. G. Smeggil, R. S. Bailey, J. C. Schuster, and H. Nowotny, High Temperatures-High Pressures, 18, 283, 1986.

7. M. K. Lewis and B. H. Attersley, Acta Metall., 13, 1163, 1965.

8. ASE Development Program Mod II: Basic Stirling Engine, Vol. I, Design Review Report, MTI Report #85TR24, April 2, 1985.

9. L. F. Coffin, Trans. ASME, 76, 931, 1954.

10. S. S. Manson, NACA Technical Note 2933, 1954.

11. C. V. Cooper and M. E. Fine, Scripta Metall., 18, 593, 1984.

12. F. D. Lemkey, H. Gupta, H. Nowotny, and S. F. Wayne, J. Mater. Sci., 19, 965, 1984.

TABLE 1

TENSILE PROPERTIES OF VARIOUSLY HEAT-TREATED, EQUIAXED NASAUT 4G-A1

Sample	Heat Treatment	Test Temp. (°C)	Ultimate Tensile Stress (MPa)	0.2% Offset Yield Stress (MPa)	Proportional Limit Stress (MPa)	Elastic Modulus (GPa)	Strain-to-Failure (%)	Reduction In Area (%)	Comments
A1-12-1	As-Cast	22	696	500	236	180	2.4	4.7	
12-3		400	543	362	223	113	5.4	8.6	
11-1		600	479	279	156	108	3.9	7.0	
12-2		800	343	248	94.5	113	8.4	17.4	
11-3		900	217	147	83.4	79.3	20.6	49.7	
A1-8-1	Under-Age	22	758	630	179	166	0.8	3.9	
8-2		400	541	390	262	139	1.8	5.5	
9-3		600	552	356	259	137	2.2	5.5	
8-3		800	337	295	123	98.6	11.6	33.4	Broke in radius
9-1		900	216	144	82.7	85.5	20.9	63.6	
A1-5-1	Super-Age	22	752	741	290	153	0.5	1.6	Broke in thread
5-2		400	612	514	259	137	1.0	3.2	
6-1		600	570	442	229	120	1.3	3.6	
5-3		800	392	287	94.5	119	9.2	23.9	
6-2		900	278	253	129	86.9	11.1	35.9	
A1-3-1	Simulated-Braze-Cycled	22	647	577	245	123	0.7	3.9	
3-2		400	521	396	179	134	1.4	2.1	
4-3		600	523	332	180	138	0.9	6.2	
3-3		800	412	276	156	105	5.7	7.0	
4-1		900	194	158	98.6	64.1	23.2	68.8	

TABLE II

LOW-CYCLE-FATIGUE DATA FOR EQUIAXED NASAUT 4G-A1

Spec. No.	Heat Treatment	Total Strain Amplitude, $\frac{\Delta\epsilon_T}{2}$(%)	Test Temp. (°C)	Cycles-to-Failure, N_f
A1-24-1	As-cast	±0.4	22	1129
22-1	"	±0.4	200	3102
20-1	"	±0.4	400	983
21-1	"	±0.4	700	800
17-2	"	±0.2	800	9412
16-2	"	±0.4	800	921
14-2	"	±0.6	800	148
15-2	"	±0.8	800	110
47-1	Simulated-	±0.4	22	100
51-1	Braze-Cycled	±0.4	200	1069
42-1	"	±0.4	400	429
41-1	"	±0.4	600	767
43-1	"	±0.4	700	730
39-1	"	±0.4	800	905
40-1	"	±0.2	800	2959
38-1	"	±0.6	800	227
37-1	"	±0.8	800	193

TABLE III

LOW-CYCLE-FATIGUE RESULTS FROM SIMULATED-BRAZE-CYCLED, EQUIAXED NASAUT 4G-A1

Specimen Number	Total Strain Amplitude, $\frac{\Delta\epsilon_T}{2}$ (%)	Cycles-to-Failure, N_f	Test Temperature (°C)
A1-25-1	±0.15	>268,310	22
A1-26-1	±0.20	6,335	22
A1-27-1	±0.25	2,892	22
A1-23-1	±0.30	284	22
A1-50-1	±0.15	11,334	800
A1-49-1	±0.20	9,628	800
A1-45-1	±0.30	1,902	800
A1-48-1	±0.40	636	800

TABLE IV
HIGH-CYCLE-FATIGUE RESULTS
FOR EQUIAXED NASAUT 4G-A1

Spec. No.	Heat Treatment	Test Temp. (°C)	σ_{max} (MPa)	Cycles-to-Failure, N_f
A1-35-1	As-Cast	22	270	1.1×10^7 +
A1-32-2	"	22	621	30.9×10^3
A1-35-1	"	200	552	1.5×10^3
A1-31-2	"	400	483	15.4×10^3
A1-32-1	"	600	316	11.9×10^6 +
A1-34-1	"	600	379	9.3×10^6 +
A1-30-2	"	600	414	240.0×10^3
A1-33-1	"	800	316	190.0×10^3
A1-58-2	Simulated-Braze-Cycled	22	621	0.3×10^3
A1-57-2	"	200	552	11.3×10^3
A1-54-1	"	400	483	46.4×10^3
A1-53-1	"	600	414	541.1
A1-36-2	"	800	316	18.6

TABLE V

TENSILE DATA FOR CARBON-MODIFIED NASAUT ALLOYS

Specimen Designation	Test Temp. (°C)	Elastic Modulus (GPa)	Proportional Limit Stress (MPa)	0.2% Offset Yield Stress (MPa)	Ultimate Tensile Stress (MPa)	Strain-to-Failure (%)
4G-A2-1	22	182.0	196.5	505.4	646.1	.875
A2-2	200	188.9	139.3	376.5	592.3	1.97
A2-3	400	152.4	196.5	357.9	568.8	2.20
A2-4	600	140.7	168.2	329.6	512.3	2.95
A2-5	800	135.1	133.1	224.8	337.2	14.3
4G-A3-1	22	184.1	167.5	438.5	724.7	2.74
A3-2	200	168.9	180.0	345.4	601.2	3.63
A3-3	400	138.6	189.6	308.9	554.4	3.95
A3-4	600	133.8	112.4	253.0	505.4	6.30
A3-5	800	174.4	83.4	215.8	309.6	8.20
4G-A4-1	22	190.3	222.9	432.0	717.8	2.15
A4-2	200	164.8	193.1	322.7	624.7	5.90
A4-3	400	168.2	176.5	291.7	617.8	8.10
A4-4	600	168.2	152.4	248.9	525.4	6.4*
A4-5	800	120.0	110.3	200.6	283.4	11.4*

* Post-test measurement

TABLE VI

LOW-CYCLE-FATIGUE RESULTS FOR CARBON-MODIFIED NASAUT 4G-A1 ALLOYS (EQUIAXED) AT 22°C

Alloy Chemistry	Total Strain Amplitude, $\frac{\Delta\epsilon_T}{2}$ (%)	Cycles-to-Failure, N_f	Failure Location
4G-A2	±0.2	7267	gauge
	±0.4	539	gauge
	±0.6	377	shoulder
	±0.8	145	at notch
4G-A3	±0.2	6577	gauge
	±0.4	1789	gauge
	±0.6	266	gauge
	±0.8	337	gauge
4G-A4	±0.2	7593	gauge
	±0.4	1181	gauge
	±0.6	480	at notch
	±0.8	289	gauge

TABLE VII

CREEP RESULTS FOR CARBON-MODIFIED NASAUT 4G-A1 ALLOYS (EQUIAXED)

Alloy	Test Temp. (°C)	Stress (MPa)	$t_{2\%}$ (hr)	t_R (hr)
4G-A2	700	345	10.1	7.1
4G-A2	800	241	*	*
4G-A2	900	103	7.0	11.3
4G-A3	700	345	0.3	0.07
4G-A3	800	241	0.02	0.01
4G-A3	900	103	1.5	20.0
4G-A4	700	345	0.3	0.3
4G-A4	800	241	0.05	18.75
4G-A4	900	103	*	*

* Failed upon loading

TABLE VIII

TENSILE PROPERTIES OF TRANSVERSELY ORIENTED, DIRECTIONALLY SOLIDIFIED NASAUT 4G–A1 IN SIMULATED–BRAZE–CYCLED CONDITION

TEST TEMPERATURE (°C)	ULTIMATE TENSILE STRESS (MPA)	0.2% OFFSET YIELD STRESS (MPA)	PROPORTIONAL LIMIT STRESS (MPA)	ELASTIC MODULUS (GPA)	STRAIN–TO–FAILURE (%)
22	514.0	357.6	154.3	187.9	0.96
200	490.6	337.0	166.1	153.5	1.25
400	441.0	311.4	198.8	126.9	1.10
600	427.2	281.1	172.9	146.6	1.45
800	264.6	192.2	111.6	105.5	7.44

TABLE IX

PLANE STRAIN FRACTURE TOUGHNESS (K_{Ic}) VALUES FOR SIMULATED-BRAZE-CYCLED, DS NASAUT 4G-A1 AT 22°C

Specimen No.	Orientation	Max. Load (kN)	Calculated K_{Ic} (MPa . $m^{1/2}$)
5078-A-01	Longitudinal (L-T)	10.0	21.0[A]
5078-A-02	Longitudinal (L-T)	4.0	10.0
5078-A-03	Transverse (T-L)	8.0	20.2
5078-A-04	Transverse (T-L)	11.3	24.3
5078-A-05	Longitudinal (L-T)	7.1	12.0[B]
5078-A-06	Transverse (T-L)	11.5	24.4

A - failed upon initial loading for precracking — K_{Ic} based on initial K_{max}.

B - failed after 2000 cycles of precracking — K_{Ic} based on K_{max} for precracking assuming zero sub-critical crack growth.

TABLE X

LOW-CYCLE-FATIGUE RESULTS AT 800°C FOR TRANSVERSELY ORIENTED, DS NASAUT 4G-A1 IN SIMULATED-BRAZE-CYCLED CONDITION

Total Strain Amplitude, $\Delta\epsilon_T/2$ (%)	Cycles-to-Failure, N_f
±0.10	1,150,000
±0.10	1,500,000
±0.15	88,540
±0.15	36,950
±0.20	3,675
±0.20	14,040
±0.20	6,650
±0.25	4,970
±0.25	1,830
±0.30	930
±0.30	1,370

TABLE XI

HIGH-CYCLE-FATIGUE RESULTS OF DS TRANSVERSE AND EQUIAXED NASAUT 4G-A1 AT 22°C

Specimen Number	Form	Heat Treatment	σ_{max} (MPa)	Cycles-to-Failure, N_f	Failure Location
5076-A-8B	DS/T	Simulated-Braze-Cycled	551	10	gauge
5077-B-8A	"	"	413	29,900	gauge
5077-A-3A	"	"	413	24,650	gauge
5076-A-9A	"	"	379	188,200	gauge
5076-A-10A	"	"	379	93,700	gauge
5077-B-8B	"	"	379	189,700	gauge
5090-03-B-4A	"	"	345	991,300	gauge
5090-03-B-4B	"	"	345	1,341,900	gauge
5076-A-4B	"	"	275	912,200	thread
5077-A-3B	"	"	275	838,860	thread
5076-A-8A	"	"	275	> 12,000,000	none
5090-03-B-8B	"	"	275	> 10,000,000	none
A1-32-2	Equiaxed	As-Cast	621	30,900	gauge
A1-35-1	"	"	270	> 11,000,000	none
A1-58-2	"	Simulated-Braze-Cycled	621	300	gauge

TABLE XII

HIGH-CYCLE-FATIGUE RESULTS OF DS TRANSVERSE AND EQUIAXED NASAUT 4G-A1 AT 200°C

Specimen Number	Form	Heat Treatment	σ_{max} (MPa)	Cycles-to-Failure, N_f	Failure Location
5090-03-B-7A	DS/T	Simulated-Braze-Cycled	413	16,700	gauge
5090-01-A-8A	"	"	413	18,100	gauge
5090-03-B-6B	"	"	379	47,000	gauge
5076-A-2A	"	"	379	101,200	gauge
5077-A-4B	"	"	379	109,100	gauge
5090-03-B-6A	"	"	345	81,100	gauge
5077-A-8A	"	"	345	185,700	gauge
5077-A-4A	"	"	275	> 10,000,000	none
5090-01-A-8B	"	"	275	> 10,000,000	none
A1-35-1	Equiaxed	As-Cast	552	1,500	gauge
A1-57-2	"	Simulated-Braze-Cycled	552	11,300	gauge

TABLE XIII

HIGH-CYCLE-FATIGUE RESULTS OF DS TRANSVERSE AND EQUIAXED NASAUT 4G-A1 AT 400°C

Specimen Number	Form	Heat Treatment	σ_{max} (MPa)	Cycles-to-Failure, N_f	Failure Location
5076-A-11A	DS/T	Simulated-Braze-Cycled	413	6,200	gauge
5090-01-A-6A	"	"	413	9,900	gauge
5077-A-8B	"	"	413	38,900	gauge
5077-B-7B	"	"	379	219,300	gauge
5090-03-B-3A	"	"	379	731,400	gauge
5090-03-B-7B	"	"	345	> 10,000,000	none
5090-03-B-1B	"	"	345	371,800	gauge
5090-03-B-2A	"	"	345	7,588,000	gauge
5090-03-B-1A	"	"	275	> 10,000,000	none
5076-A-3A	"	"	275	8,900,000	gauge
A1-31-2	Equiaxed	As-Cast	483	15,400	gauge
A1-54-1	"	Simulated-Braze-Cycled	483	46,400	gauge

TABLE XIV

HIGH-CYCLE-FATIGUE RESULTS OF EQUIAXED NASAUT 4G-A1 AT 800°C

Specimen Number	Heat Treatment	σ_{max} (MPa)	Cycles-to-Failure, N_f	Failure Location
9-1	Simulated-Braze-Cycled	310	9,500	gauge
9-2	"	310	5,500	gauge
9-3	"	293	24,200	gauge
9-4	"	293	14,700	gauge
9-5	"	276	31,500	gauge
9-6	"	276	32,100	gauge
9-7	"	265	42,700	gauge
9-8	"	265	120,600	gauge
9-9	"	241	164,100	gauge
9-10	"	241	179,000	gauge
A1-33-1	As-Cast	316	190,000	gauge
A1-36-2	Simulated-Braze-Cycled	316	9,500	gauge

TABLE XV

HIGH-CYCLE-FATIGUE RESULTS OF DS TRANSVERSE AND EQUIAXED NASAUT 4G-A1 AT 600°C

Specimen Number	Form	Heat Treatment	σ_{max} (MPa)	Cycles-to-Failure, N_f	Failure Location
5076-A-13	DS/T	Simulated-Braze-Cycled	413	181,700	gauge
5077-A-9A	"	"	413	148,500	gauge
5077-A-12A	"	"	413	166,100	gauge
5090-03-B-8A	"	"	379	235,100	gauge
5077-A-11B	"	"	379	174,200	gauge
5090-03-B-2B	"	"	345	6,643,100	gauge
5076-A-4A	"	"	345	7,414,300	gauge
5076-A-11B	"	"	279	> 10,000,000	none
A1-30-2	Equiaxed	As-Cast	414	240,000	gauge
A1-53-1	"	Simulated-Braze-Cycled	414	8,000	gauge

TABLE XVI

HIGH-CYCLE-FATIGUE RESULTS OF DS TRANSVERSE AND EQUIAXED NASAUT 4G-A1 AT 800°C

Specimen Number	Form	Heat Treatment	σ_{max} (MPa)	Cycles-to-Failure, N_f	Failure Location
5076-A-12	DS/T	Simulated-Braze-Cycled	276	19,300	gauge
5090-01-A-6B	"	"	276	77,200	gauge
5090-03-B-3B	"	"	241	38,300	gauge
5077-A-11A	"	"	241	12,000	gauge
5077-B-7A	"	"	207	150,500	gauge
5077-A-2	"	"	207	165,400	gauge
5077-A-1	"	"	138	> 10,500,000	none
5077-A-12B	"	"	138	> 10,000,000	none
A1-33-1	Equiaxed	As-Cast	316	190,000	gauge
A1-36-2	"	Simulated-Braze-Cycled	316	9,500	gauge

TABLE XVII

CREEP RESULTS FOR SIMULATED-BRAZE-CYCLED DS/L NASAUT 4G-A1 AT 800°C

Specimen Number	Stress (MPa)	Time (hr) to % Creep of 0.1	0.5	1.0	2.0	t_R (hrs)	Final Creep Strain (%)
5301-6	50	14	-	-	-	503.4(c)(d)	0.39
5076-11B	50	14	51	-	-	543.5(c)	0.52
5076-14T	86	.24	4.5	15	47	66.4(c)	2.61
5076-14B	86	.24	3.1	12	38	65.7(c)	3.06
5301-13	120	.01	.29	1.2	2.8	18.8(b)	-
5076-15B	120	.03	.30	.91	2.4	14.0(a)	-

Notes:

(a) Specimen failed at time shown. Final elongation = 41.5%, % R.A. = 46.6

(b) Specimen failed at time shown. Final elongation = 42.5%, % R.A. = 64.0

(c) Specimen unloaded without failure at time shown

(d) Specimen broke while removing from adapter

TABLE XVIII

LOW-CYCLE-FATIGUE RESULTS FOR SIMULATED-BRAZE-CYCLED NASAUT 4G-A1

Specimen Number	Form	Total Strain Amplitude, $\frac{\Delta\epsilon_T}{2}$ (%)	Cycles-to-Failure, N_f	Test Temperature (°C)
5301-7	DS/L	±0.10	41,101	22
5301-8	"	±0.10	>218,300	22
5078-1	"	±0.15	26,362	22
5078-2	"	±0.15	24,362	22
5076-2	"	±0.25	14,539	22
5076-3	"	±0.25	4,845	22
5078-7	"	±0.30	44	22
5078-12	"	±0.30	95	22
5301-2	"	±0.10	>203,650	400
5078-4	"	±0.10	>307,900	400
5078-10	"	±0.15	35,966	400
5301-11	"	±0.15	>101,560	400
5076-1	"	±0.30	3,023	400
5301-4	"	±0.30	2,714	400
5076-4	"	±0.40	539	400
5301-9	"	±0.40	748	400
5301-12	"	±0.15	>337,300	800
5301-14	"	±0.15	>262,295	800
5301-3	"	±0.30	1,599	800
5301-10	"	±0.30	6,092	800
5078-3	"	±0.40	1,166	800
5078-5	"	±0.40	1,390	800
5078-9	"	±0.50	473	800
5078-11	"	±0.50	392	800
A1-24-1	Equiaxed	±0.40	100	22
A1-42-1	"	±0.40	429	400
A1-40-1	"	±0.20	2,959	800
A1-39-1	"	±0.40	905	800

TABLE XIX

HIGH-CYCLE-FATIGUE FOR SIMULATED-BRAZE-CYCLED DS/L NASAUT 4G-A1

Specimen Number	σ_{max} (MPa)	Cycles-to-Failure, N_f	Test Temperature (°C)
5301-17	241	141,632	22
5301-31	241	> 10,475,000	22
5301-24	264	> 10,000,000	22
5301-25	264	> 10,000,000	22
5301-22	287	86,952	22
5301-15	287	167,170	22
5301-20	310	995,708	22
5301-34	310	114,856	22
5301-27	241	> 10,039,804	400
5301-25B	241	> 10,000,200	400
5076-12T	287	> 10,221,000	400
5301-29	287	> 11,211,000	400
5301-23	310	> 10,000,009	400
5301-33A	310	177,822	400
5076-15T	310	> 10,000,000	400
5301-25B*	333	73,652	400
5301-29**	360	38,307	400
5301-18***	376.5	7,406,593	400
5301-26	241	41,397	800
5076-11B	241	141,800	800
5301-16	264	17,251	800
5301-19	264	42,732	800
5076-10B	287	15,323	800
5076-11T	287	13,423	800
5301-33B	310	4,635	800
5301-20-2	310	5,042	800

* Reloaded following > 10,000,200 cycles at 241 MPa and 400°C

** Reloaded following > 11,211,000 cycles at 287 MPa abnd 400°C

*** Reloaded following > 3,162,414 cycles at 360 MPa and 400°C

TABLE XX

TENSILE PROPERTIES OF SIMULATED-BRAZE-CYCLED, DS/L NASAUT 4G-A1

Specimen Identification	Test Temp. (°C)	Elastic Modulus (GPa)	Ultimate Tensile Stress (MPa)	0.2% Offset Yield Stress (MPa)	Strain-to-Failure (%)	Reduction-in-Area (%)
5076-13T	22	131.6	507	369	1.0	1.1
5301-32	22	135.7	617	514	0.8	0
5076-17T*	200	113.0	395	338	0.8	0
5076-18T*	200	128.2	411	320	0.7	0.8
5076-12B	400	113.0	451	328	1.6	0.6
5076-13B	400	112.3	447	336	1.5	0.6
5078-6*	600	92.3	410	294	1.6	1.0
5301-1*	600	115.8	451	280	3.1	2.1
5078-8*	800	73.7	240	186	29.8	37.3
5301-5*	800	76.5	268	192	19.3	27.1

* Tested at 0.005 min^{-1} strain rate; all others tested at 0.05 min^{-1} strain rate

Fe-Mn-Cr-Al-C ALLOY ITERATION FLOW CHART

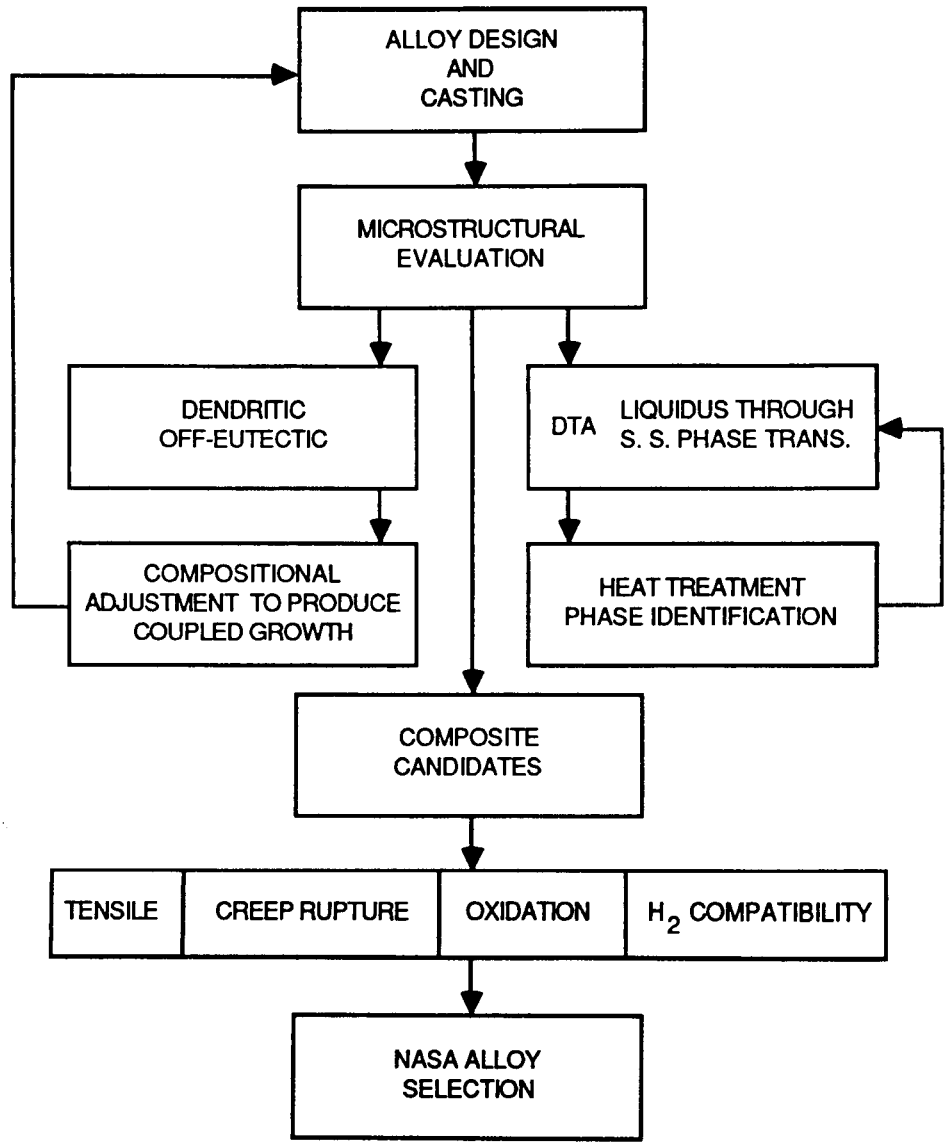

FIG. 2

LARSON-MILLER RUPTURE CURVES FOR NASAUT 4G MODIFICATIONS

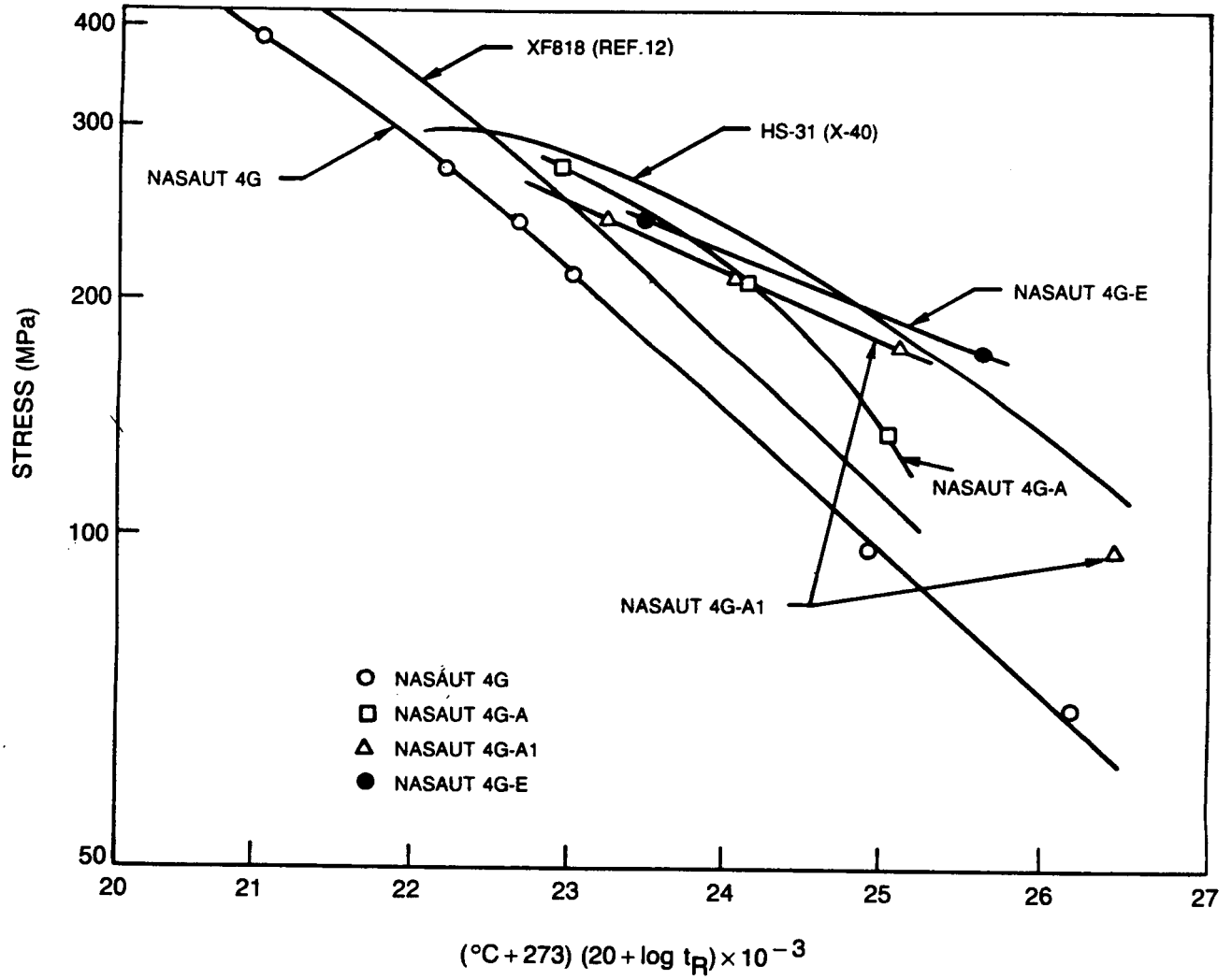

FIG. 3

ORIGINAL PAGE IS
OF POOR QUALITY

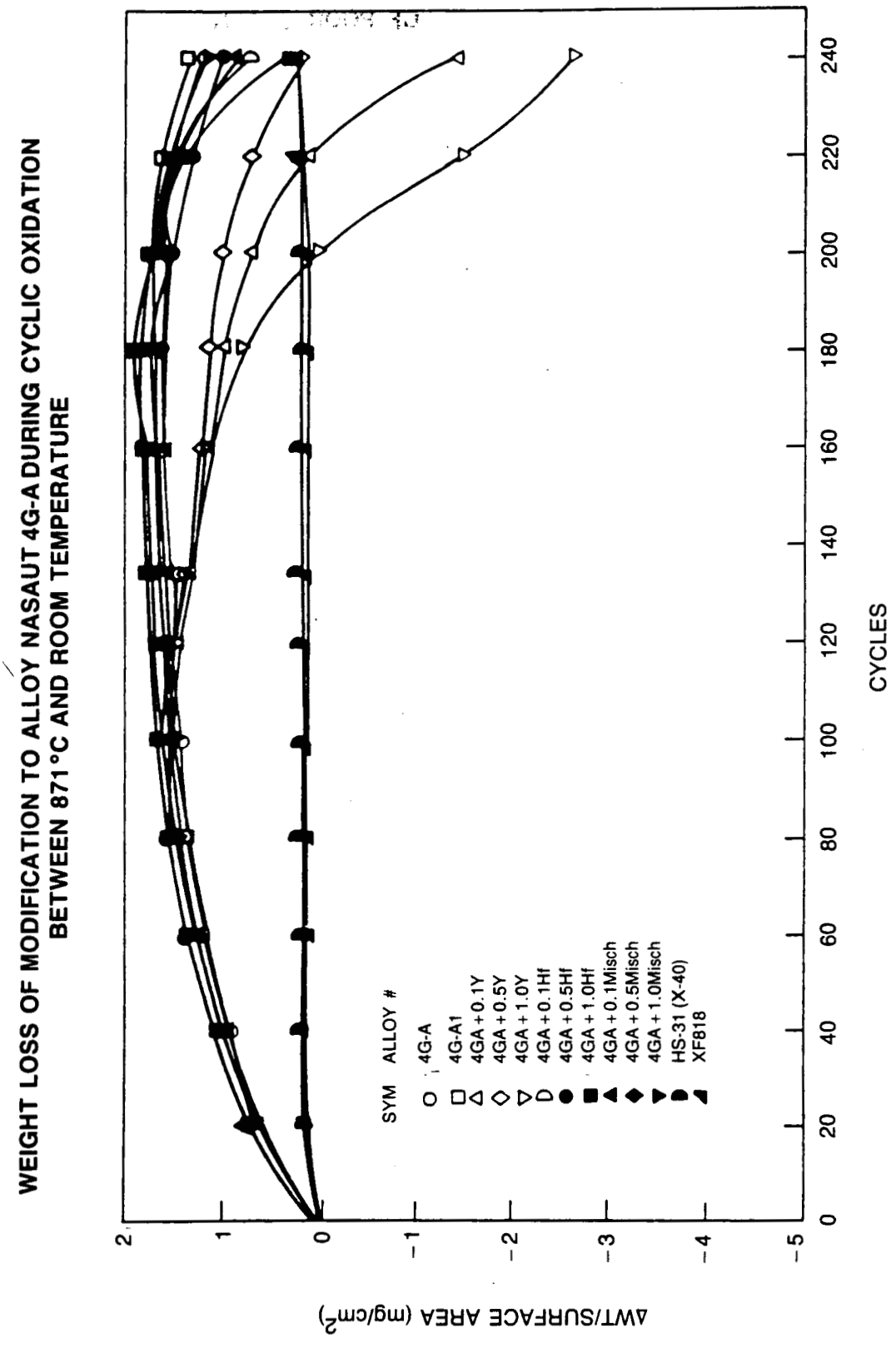

89—6—8—4

GASEOUS OXIDATION TESTING OF FERROUS/COBALT STIRLING ENGINE HEATER HEAD ALLOYS

(AFTER 383 HOURS AT 871 °C WITH 35ppm $NaCl_{(g)}$ IN AIR)

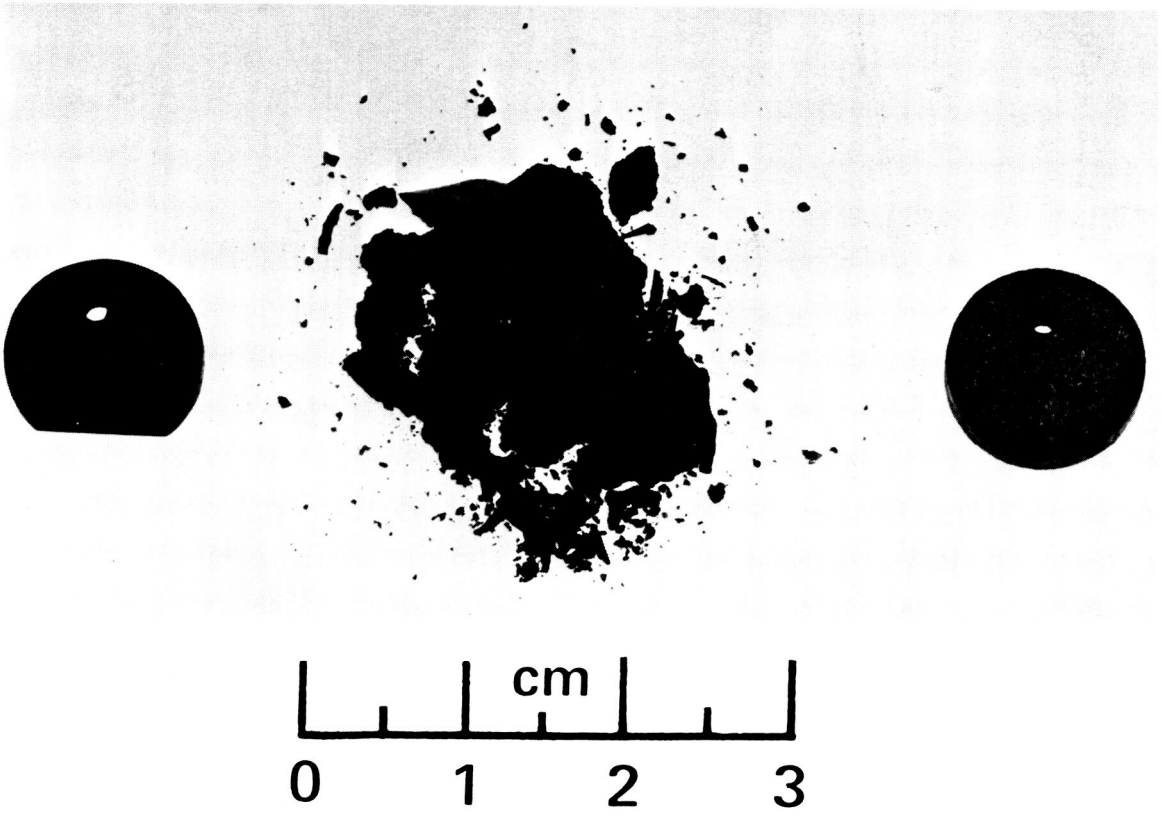

HS-31 (X-40) XF 818 NASAUT 4G-A1

84–7–35–17

FIG. 5

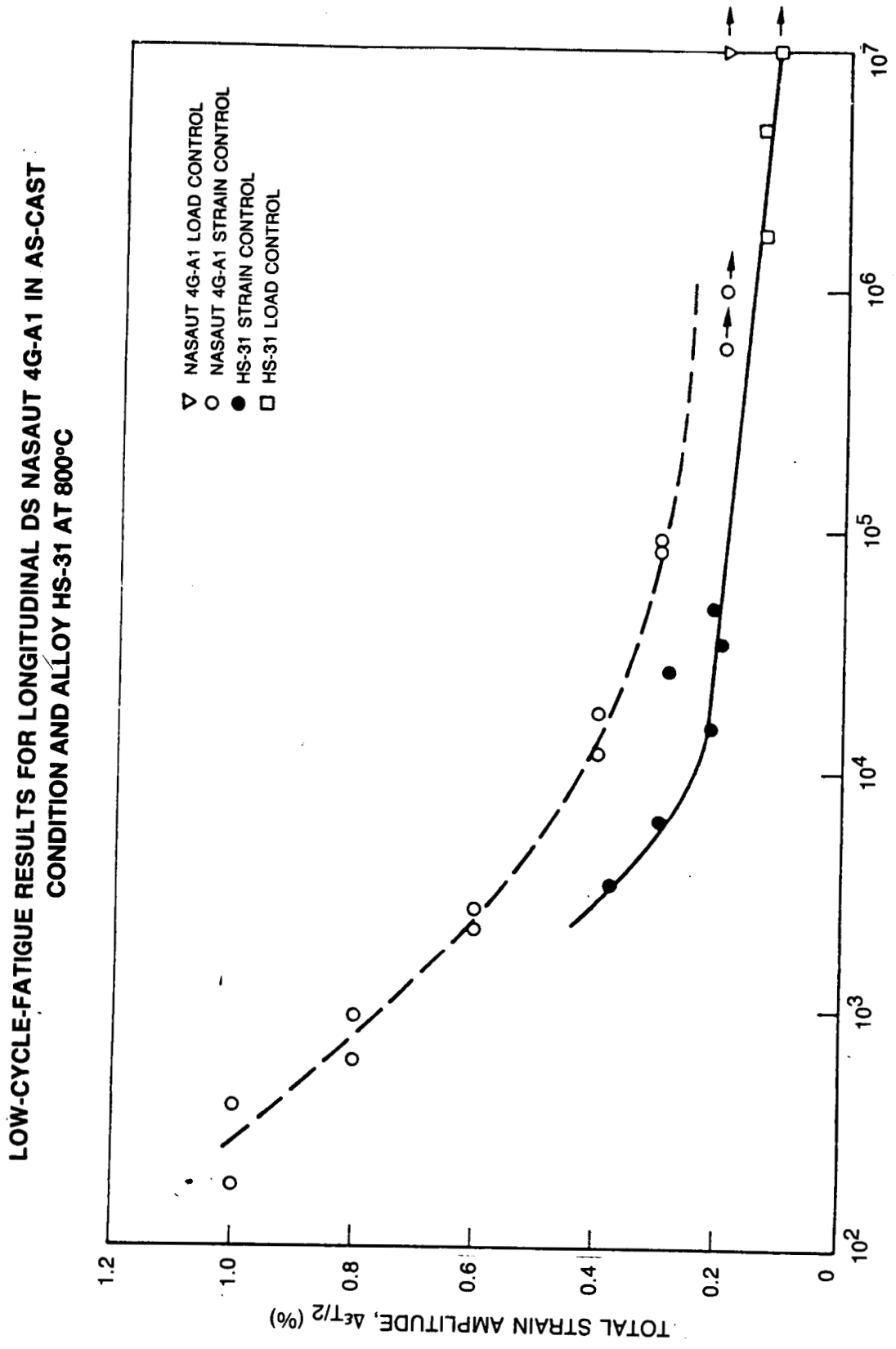
LOW-CYCLE-FATIGUE RESULTS FOR LONGITUDINAL DS NASAUT 4G-A1 IN AS-CAST CONDITION AND ALLOY HS-31 AT 800°C
NASAUT 4G-A1 LOAD CONTROL
NASAUT 4G-A1 STRAIN CONTROL
HS-31 STRAIN CONTROL
HS-31 LOAD CONTROL
TOTAL STRAIN AMPLITUDE, $\Delta\varepsilon_{T/2}$ (%)
1.2
1.0
0.8
0.6
0.4
0.2
0
10^2
10^3
10^4
10^5
10^6
10^7
CYCLES-TO-FAILURE, N_f

89—6—8—3

FIG. 6

MICROSTRUCTURE OF NASAUT 4G-A1

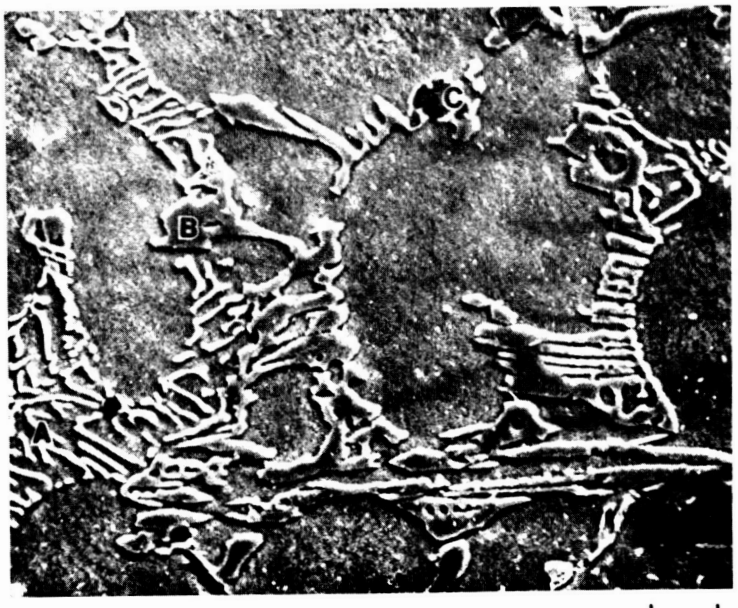

a)

10μm

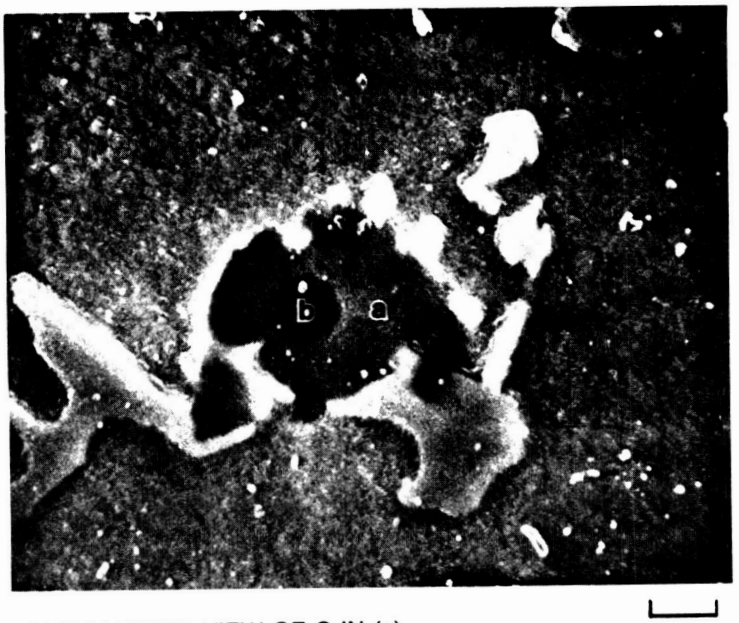

b) MAGNIFIED VIEW OF C IN (a)

2μm

89—6—8—11

FIG. 7

AGE-HARDENING RESPONSE FOR ALLOY NASAUT 4G-A1

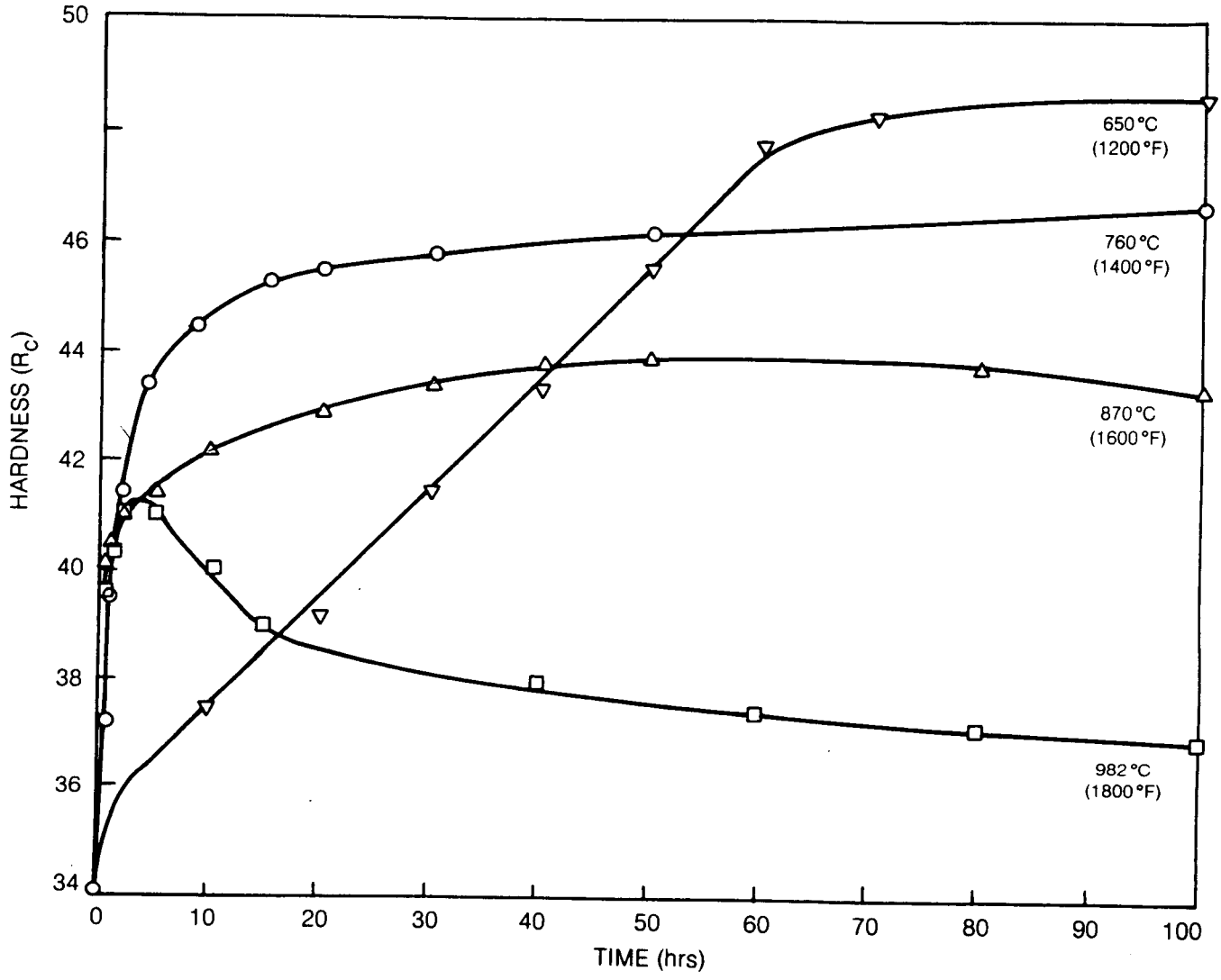

89—6—8—8

ORIGINAL PAGE
BLACK AND WHITE PHOTOGRAPH

FIG. 8

ORIGINAL PAGE IS
OF POOR QUALITY

UNDER-AGED MICROSTRUCTURE SHOWING THICK PLATES OF $M_{23}C_6$ AND MATRIX STACKING FAULTS, SOME TERMINATING AT PARTIAL DISLOCATIONS

(870°C/8 hr/WQ)

89—6—8—10

FIG. 9

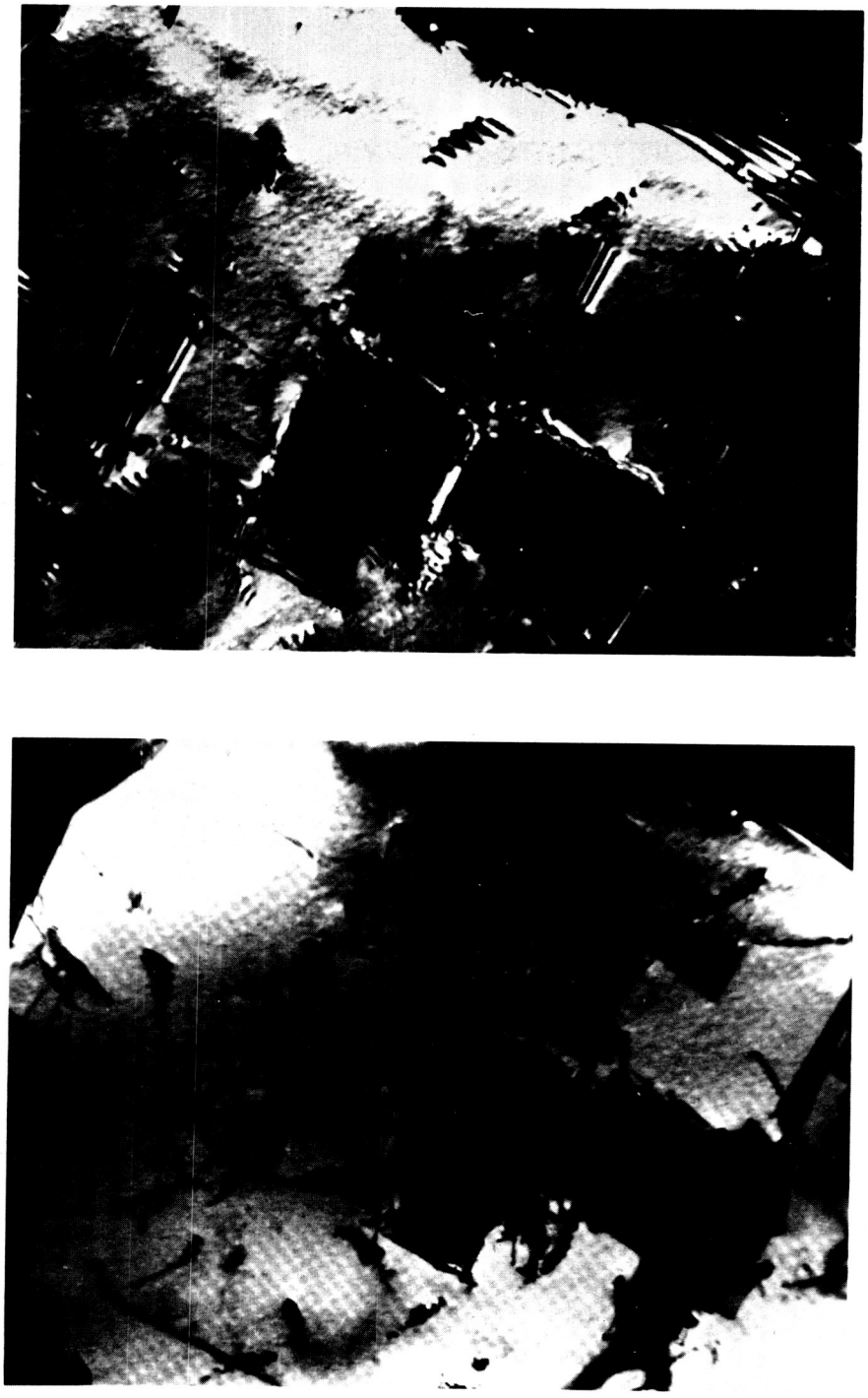

89—6—8—9

FIG. 10

EFFECT OF HEAT TREATMENT ON YIELD STRESS FOR NASAUT 4G-A1

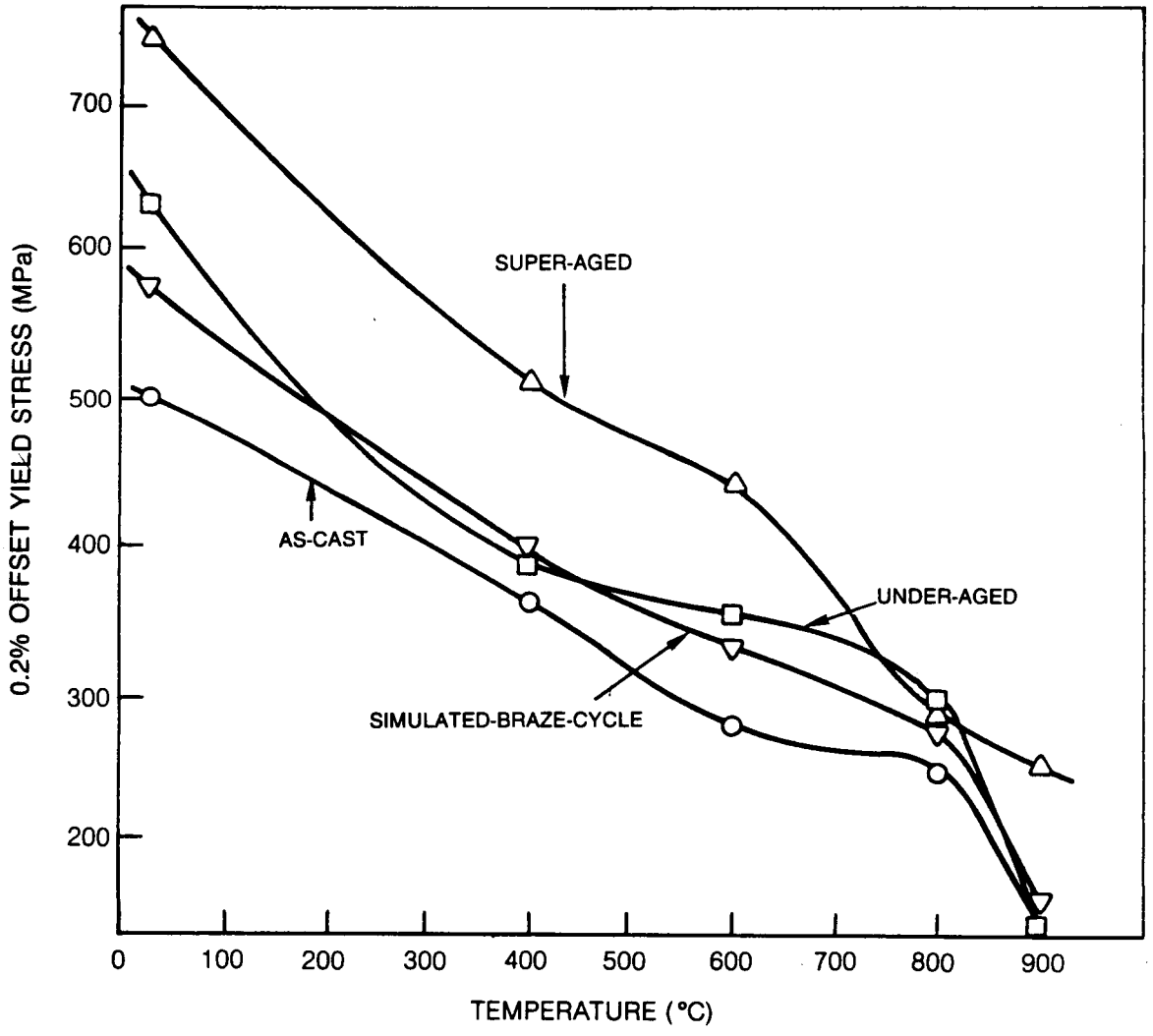

89-6-8-7

EFFECT OF HEAT TREATMENT ON STRAIN-TO-FAILURE FOR NASAUT 4G-A1

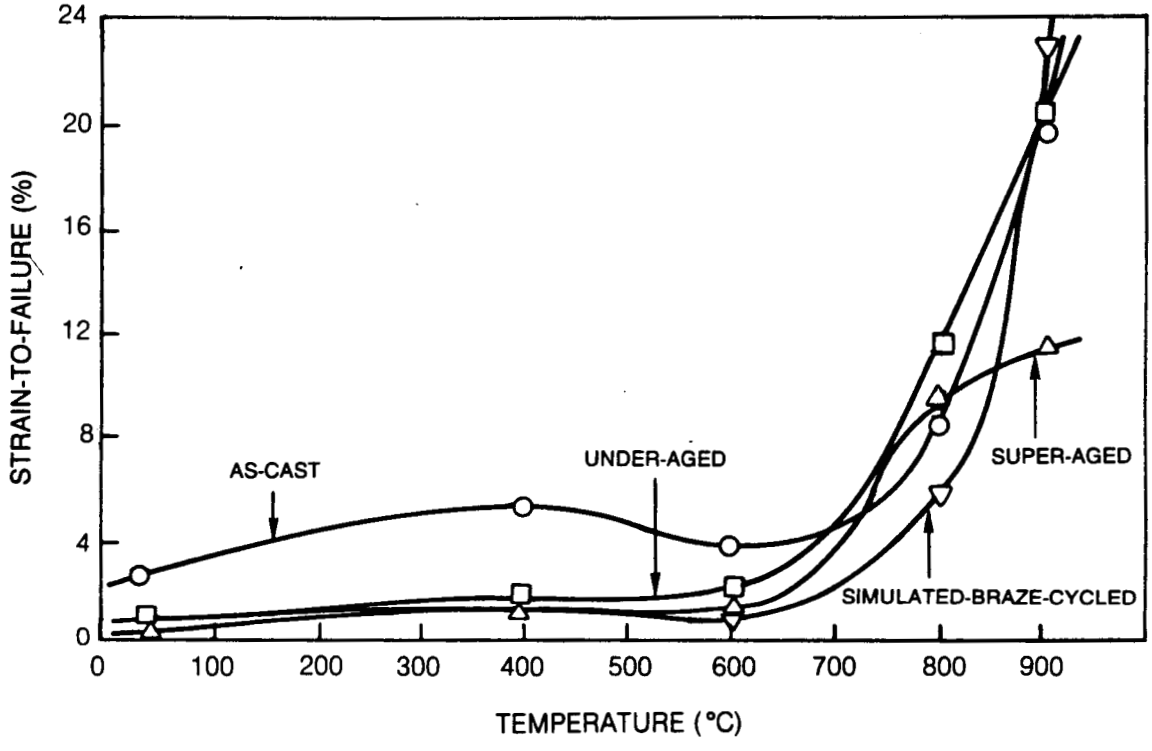

COMPARISON OF STRENGTH AND STRAIN-TO-FAILURE BETWEEN NASAUT 4G-A1 AND XF-818

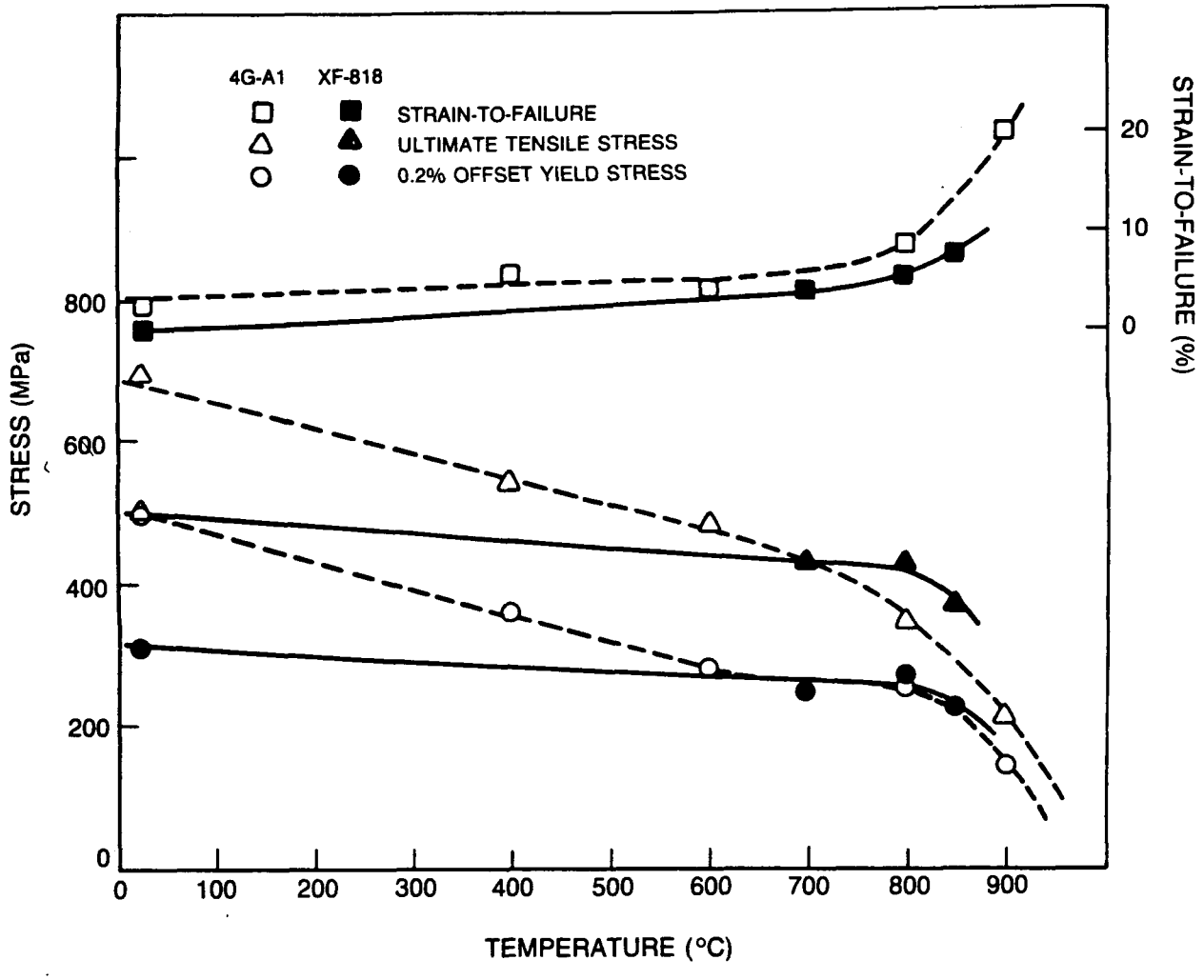

FIG. 13

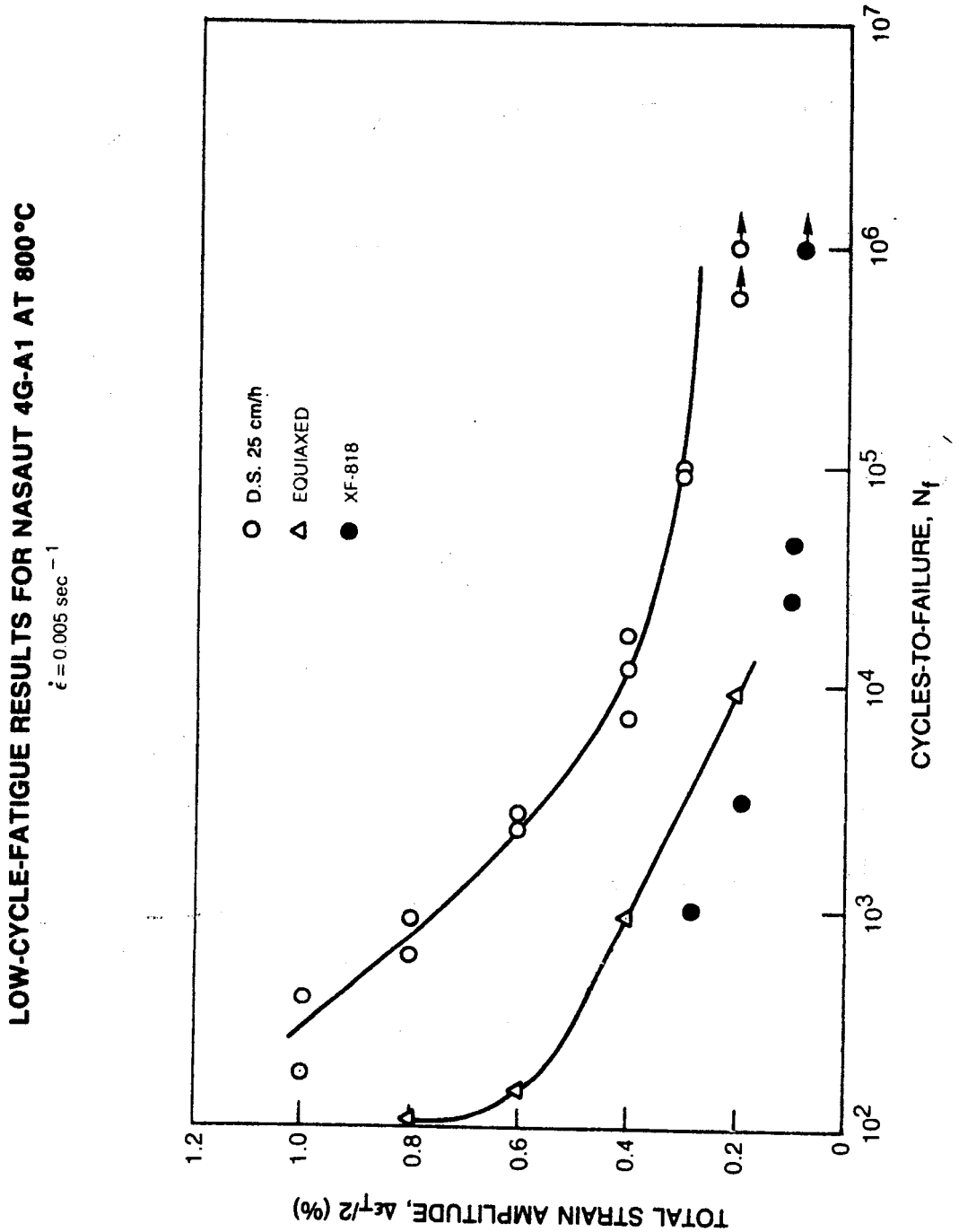
LOW-CYCLE-FATIGUE RESULTS FOR NASAUT 4G-A1 AT 800°C
$\dot{\epsilon} = 0.005\ sec^{-1}$
O D.S. 25 cm/h
Δ EQUIAXED
● XF-818
TOTAL STRAIN AMPLITUDE, $\Delta\epsilon_T/2$ (%)
1.2
1.0
0.8
0.6
0.4
0.2
0
10^2
10^3
10^4
10^5
10^6
10^7
CYCLES-TO-FAILURE, N_f

FIG. 14

LOW-CYCLE FATIGUE OF NASAUT 4G-A1 EQUIAXED CASTINGS TESTED AT 800°C

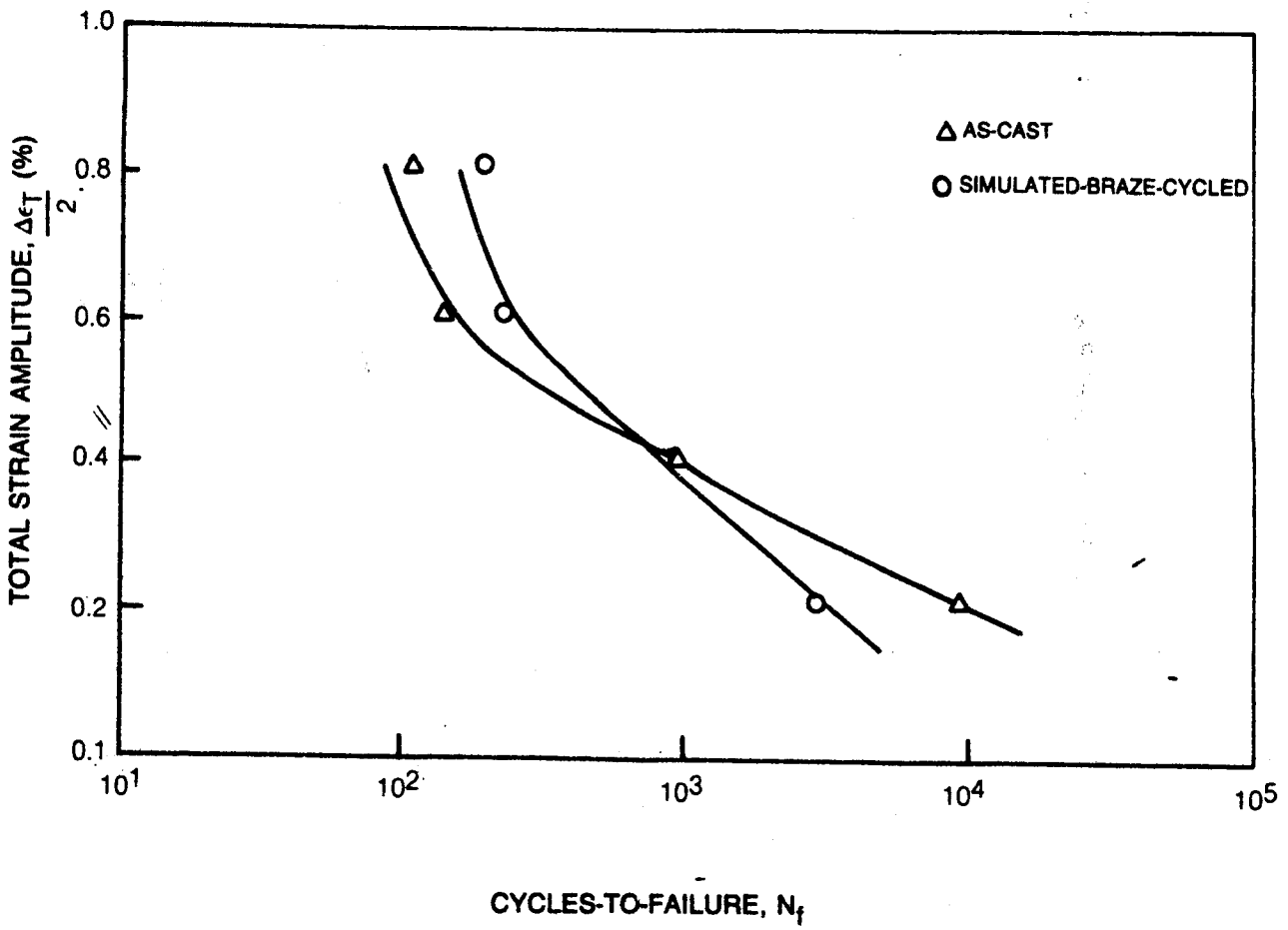

FIG. 15

LOW-CYCLE FATIGUE OF NASAUT 4G-A1 EQUIAXED CASTINGS

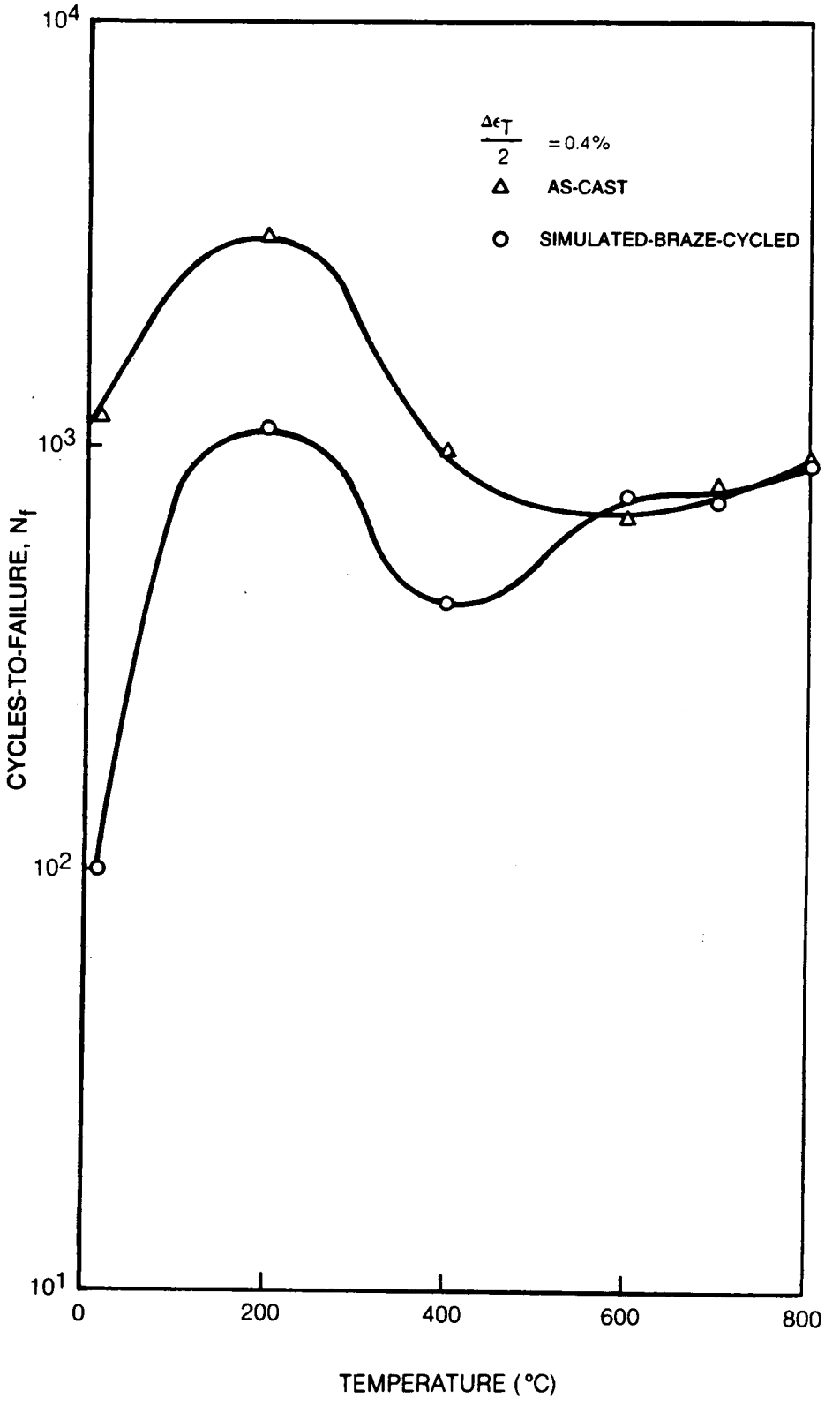

85-6-6-2

FIG. 16

LOW-CYCLE FATIGUE OF SIMULATED-BRAZE-CYCLED, EQUIAXED NASAUT 4G-A1

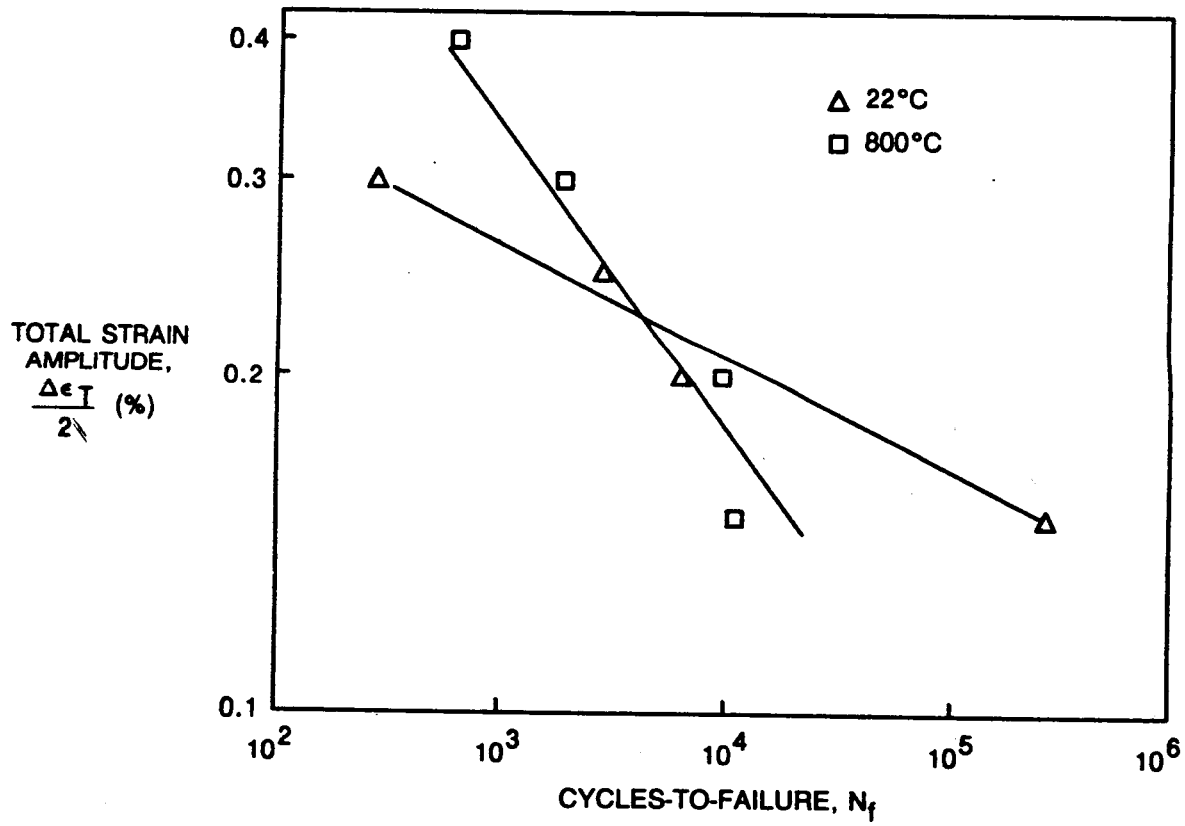

89-3-50-7

FIG. 17

HIGH-CYCLE FATIGUE OF VARIOUSLY HEAT-TREATED NASAUT 4G-A1 AT 800°C

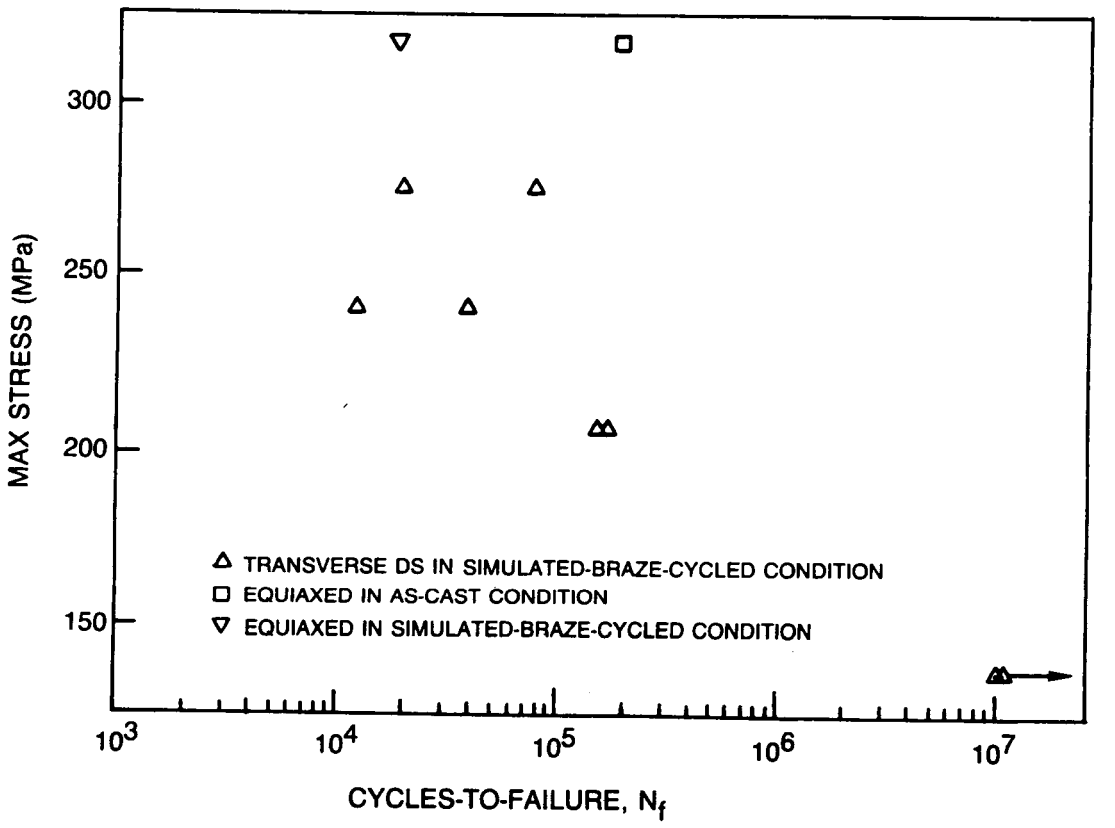

FIG. 18

OPTICAL MICROGRAPHS OF EQUIAXED NASAUT ALLOYS IN THE AS-CAST CONDITION

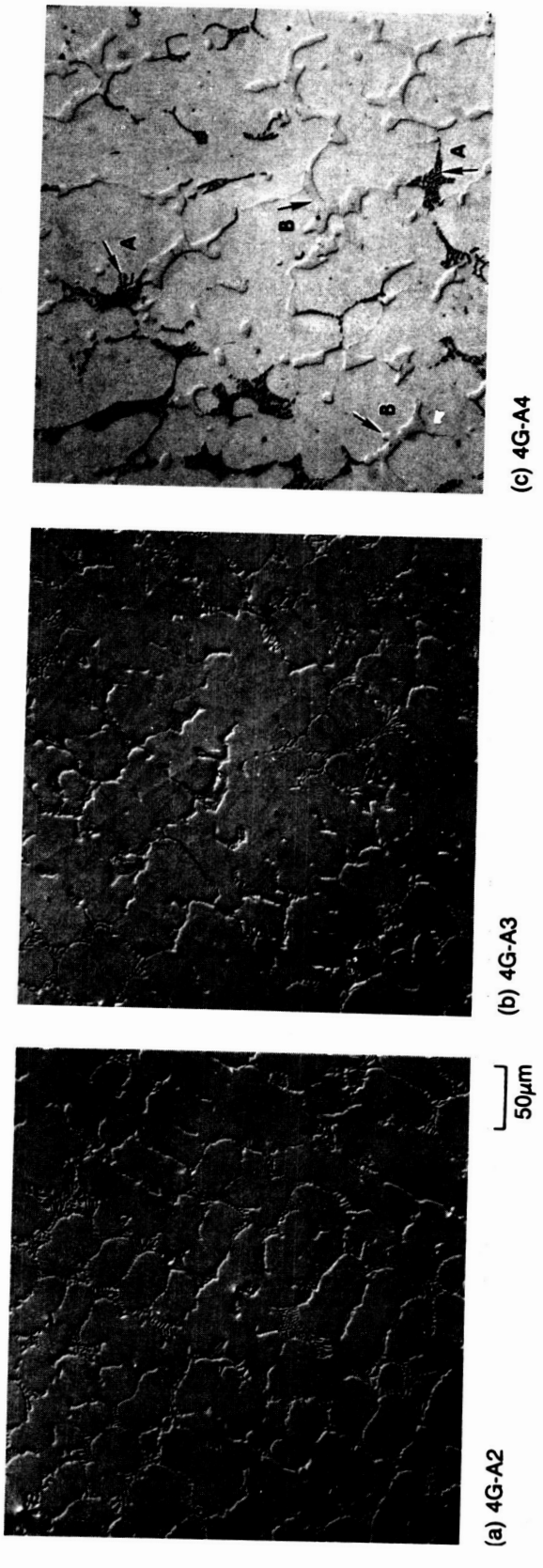

(c) 4G-A4

(b) 4G-A3

(a) 4G-A2

86-5-5-1

FIG. 19

OPTICAL MICROGRAPHS OF EQUIAXED NASAUT ALLOYS IN THE SIMULATED-BRAZE-CYCLED CONDITION

(1065°C/30 min. + 790°C/16 hr + 650°C/16 hr)

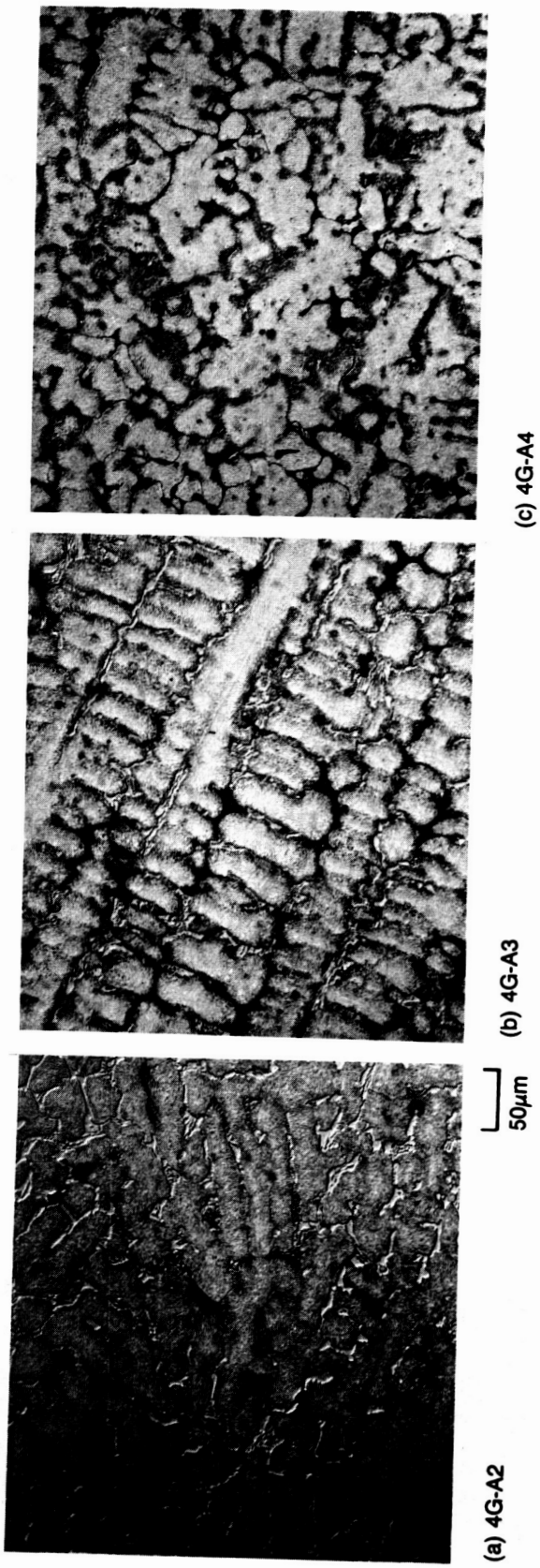

86-5-5-2

FIG. 20

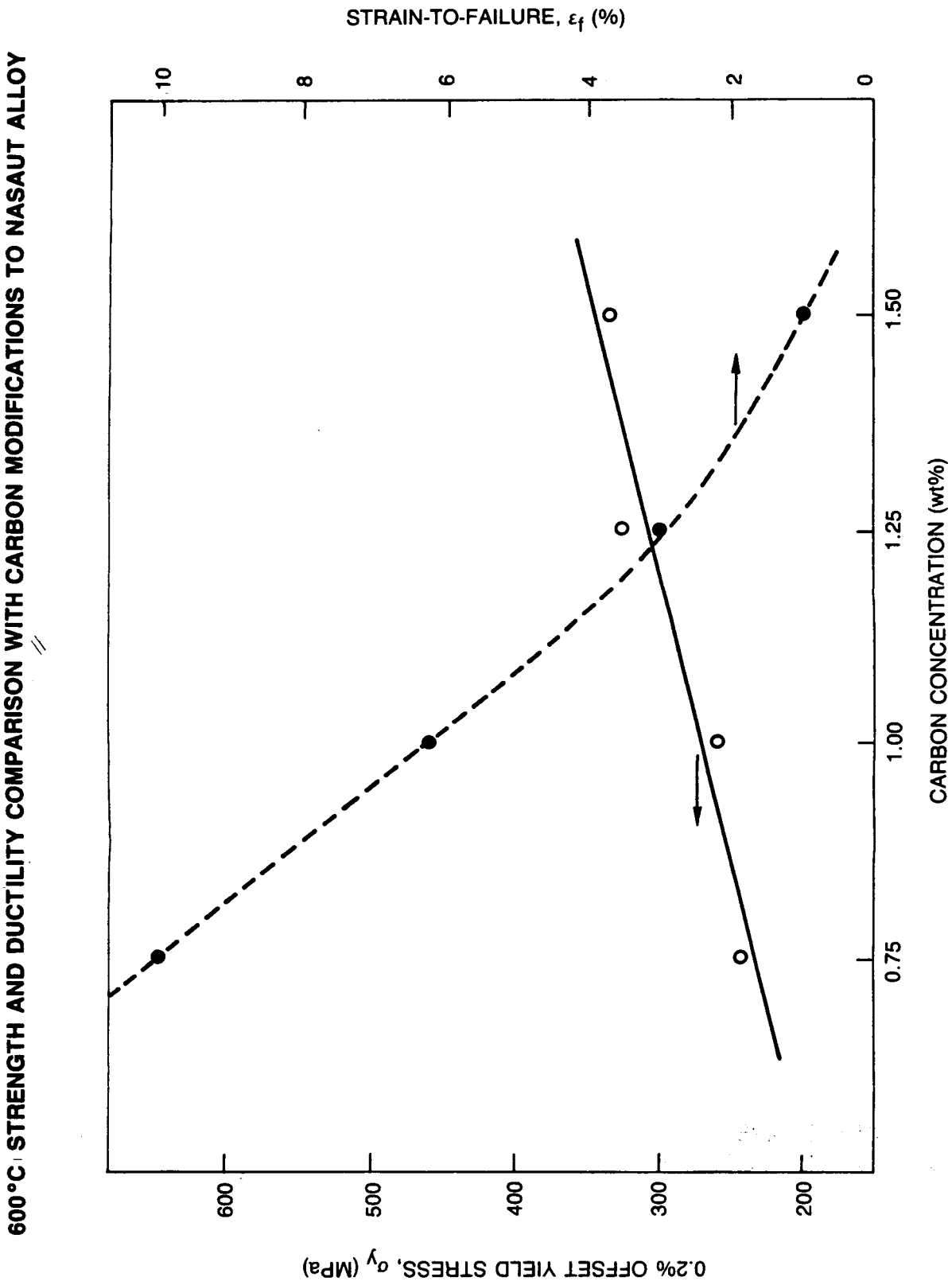

86-5-20-6

FIG. 21

800°C LOW-CYCLE-FATIGUE DATA FOR SIMULATED-BRAZE-CYCLED CARBON MODIFIED ALLOYS

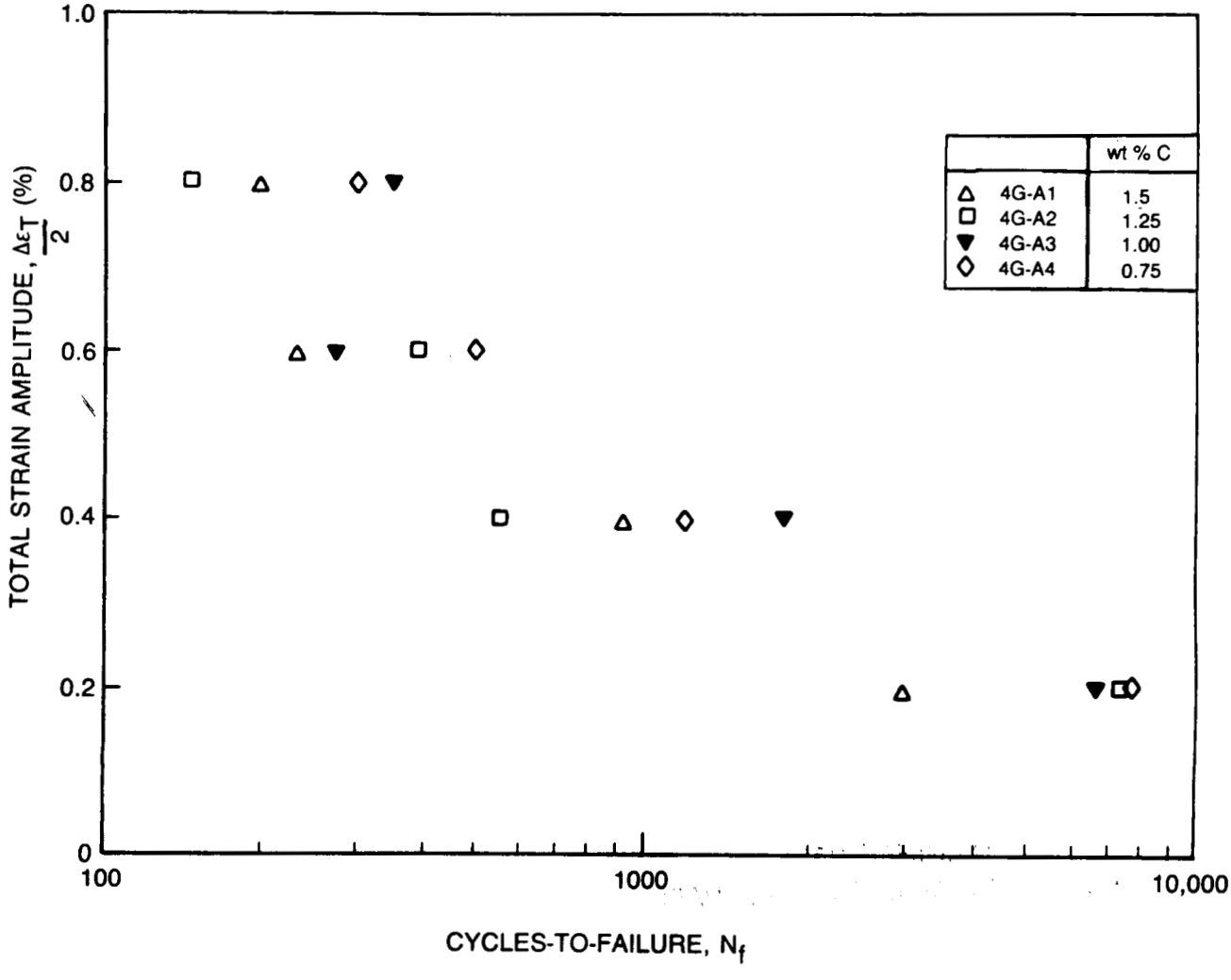

86-11-42-1

FIG. 22

OPTICAL MACROGRAPH OF DIRECTIONALLY SOLIDIFIED NASAUT 4G-A1 IN AS-CAST CONDITION

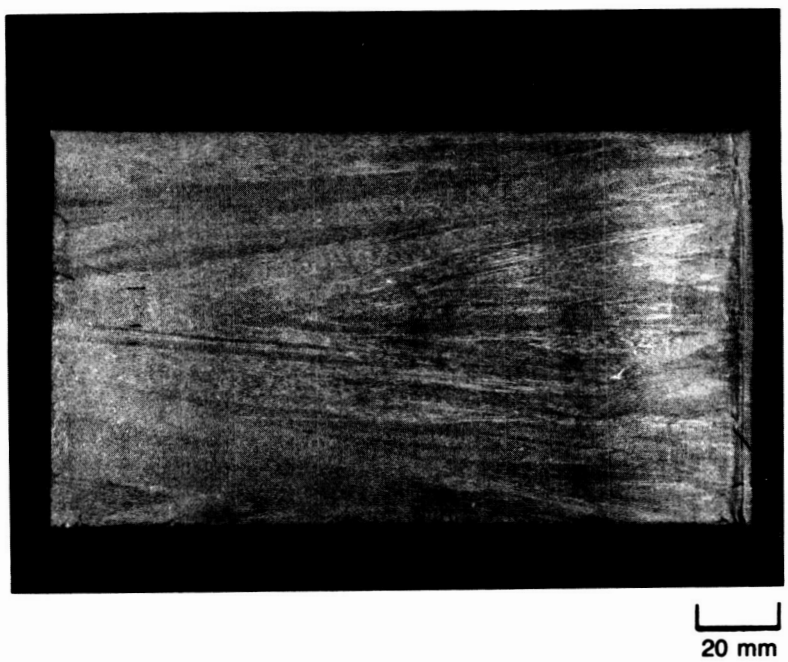

87-2-23-1

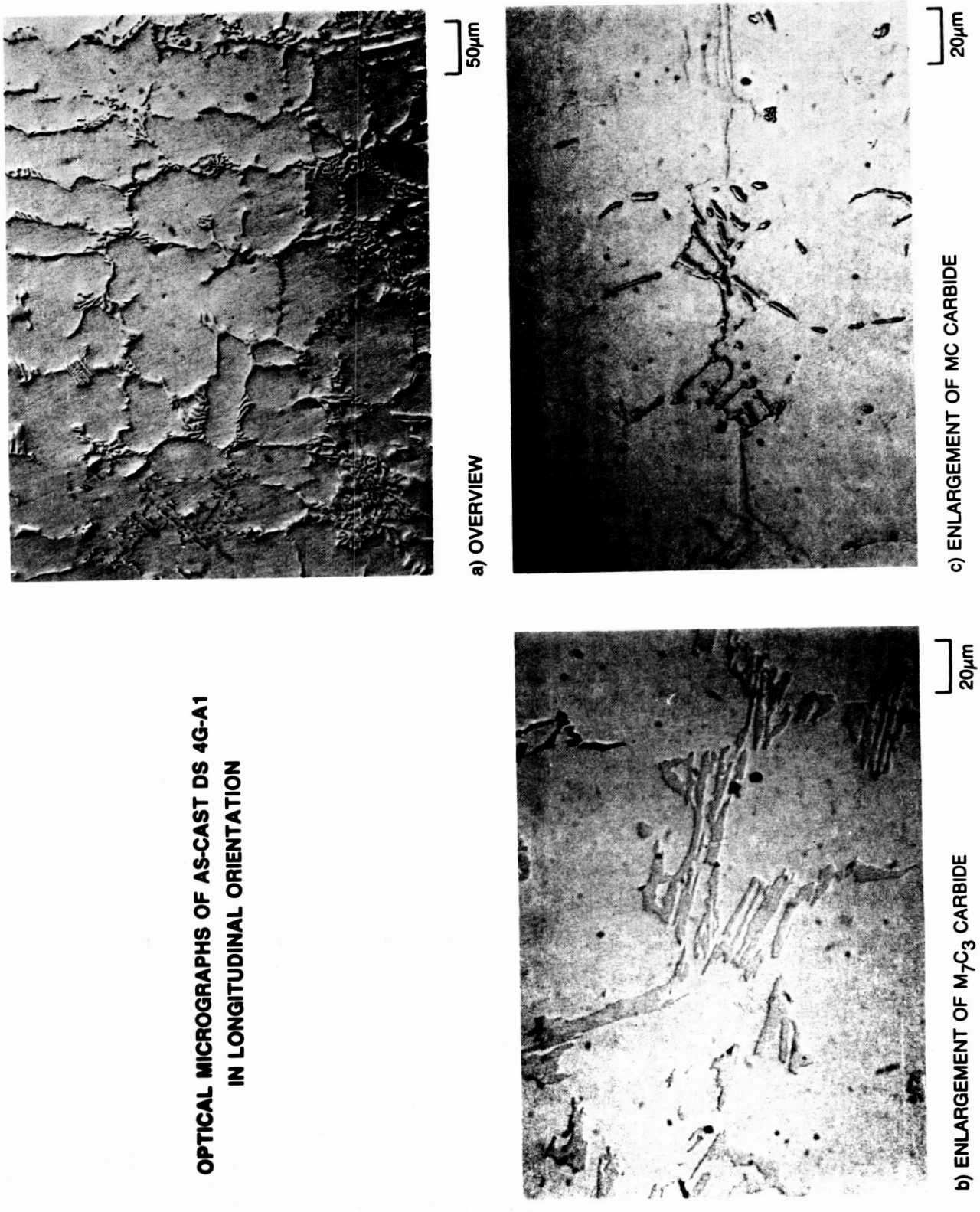

OPTICAL MICROGRAPHS OF AS-CAST DS 4G-A1 IN LONGITUDINAL ORIENTATION

87-3-22-1

FIG. 24

0.2% OFFSET YIELD STRESS AS A FUNCTION OF TEMPERATURE FOR TRANSVERSELY ORIENTED, DS NASAUT 4G-A1 IN SIMULATED-BRAZE-CYCLED CONDITION

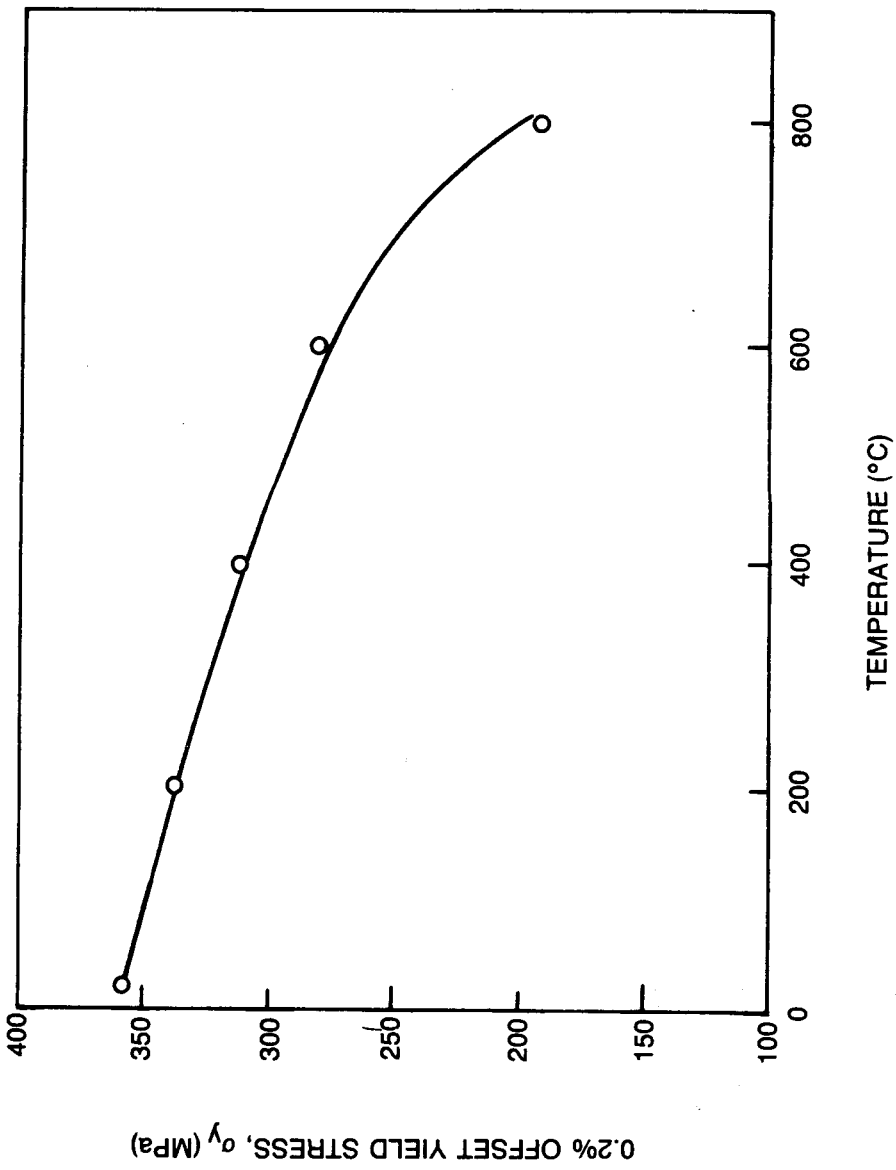

STRAIN-TO-FAILURE AS A FUNCTION OF TEMPERATURE FOR TRANSVERSELY ORIENTED, DS NASAUT 4G-A1 IN SIMULATED-BRAZE-CYCLED CONDITION

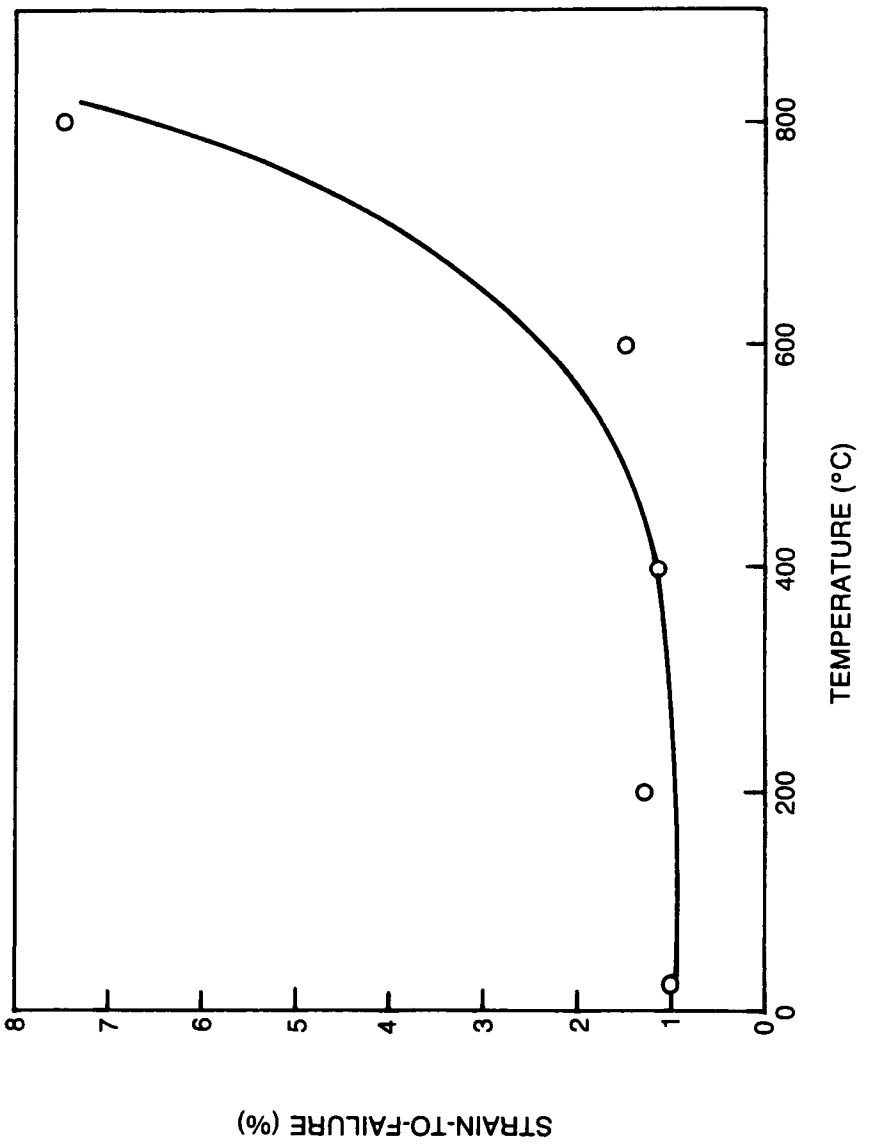

SCHEMATIC ILLUSTRATION OF ORIENTATION RELATIONSHIP BETWEEN DS DIRECTION AND CRACK PROPAGATION PLANE

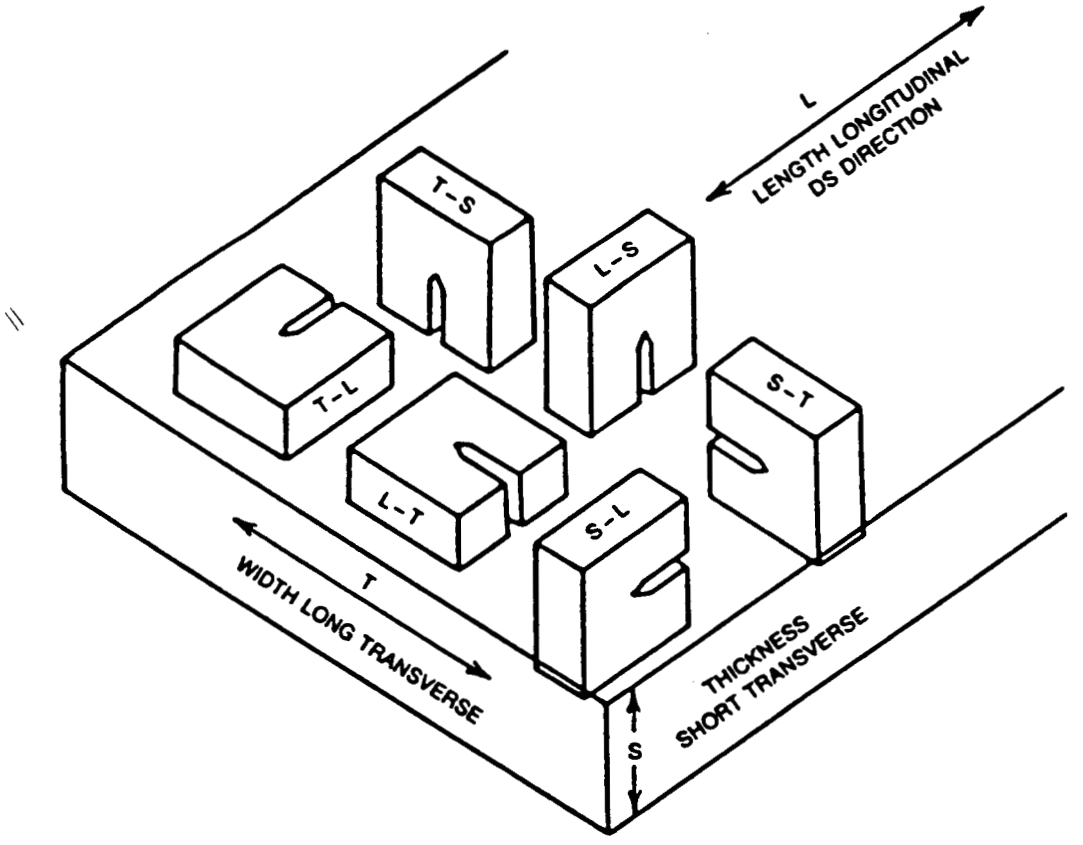

FIG. 27

LOW-MAGNIFICATION SEM FRACTOGRAPHS OF SIMULATED-BRAZE-CYCLED DS NASAUT 4G-A1 FRACTURE TOUGHNESS SPECIMENS

a) TRANSVERSE (T-L) ORIENTATION

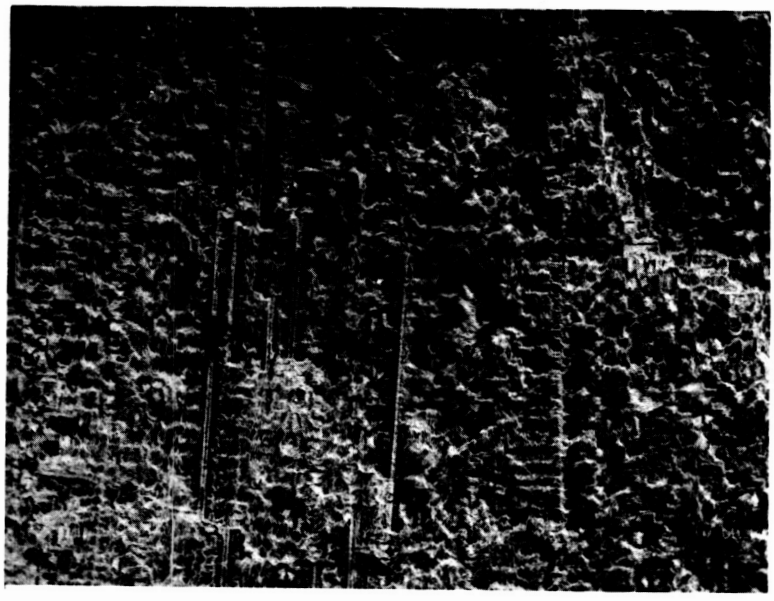

1 mm

b) LONGITUDINAL (L-T) ORIENTATION

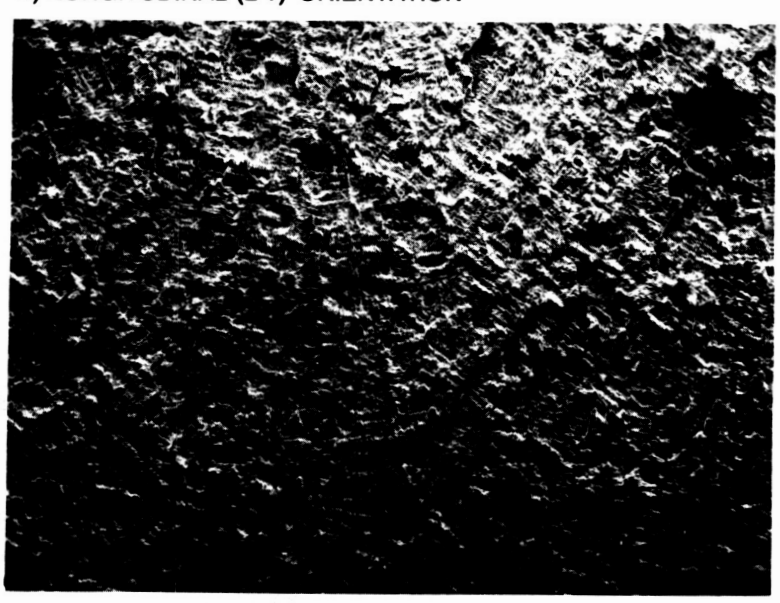

1 mm

87-9-16-2

HIGHER-MAGNIFICATION SEM FRACTOGRAPHS OF SIMULATED-BRAZE-CYCLED DS NASAUT 4G-A1 FRACTURE TOUGHNESS SPECIMENS

a) TRANSVERSE (T-L) ORIENTATION

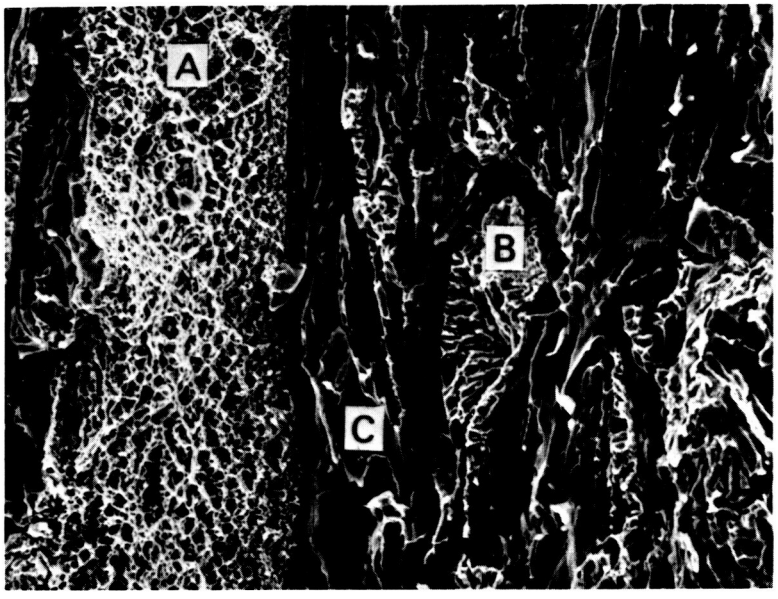

b) LONGITUDINAL (L-T) ORIENTATION

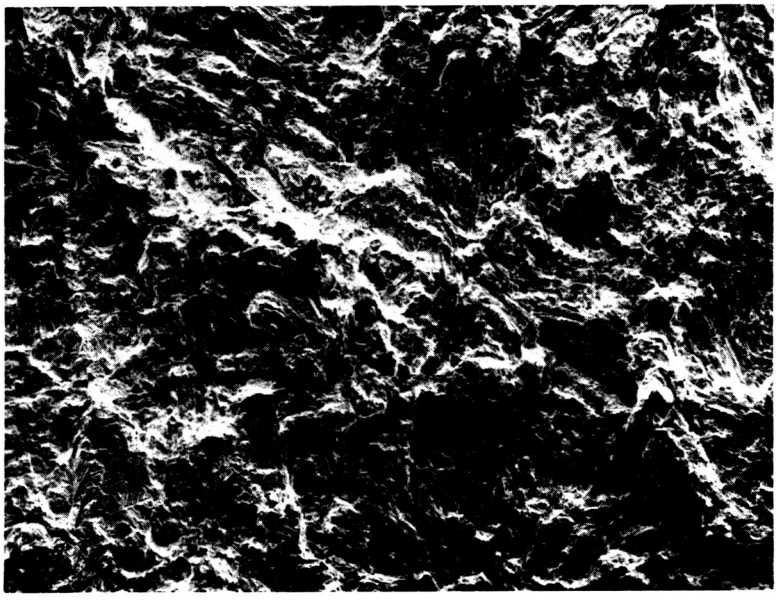

87-9-16-3

SCHEMATIC REPRESENTATION OF FRACTURE TOUGHNESS SPECIMEN AND RELATIONSHIP TO METALLOGRAPHICALLY EXAMINED SURFACE

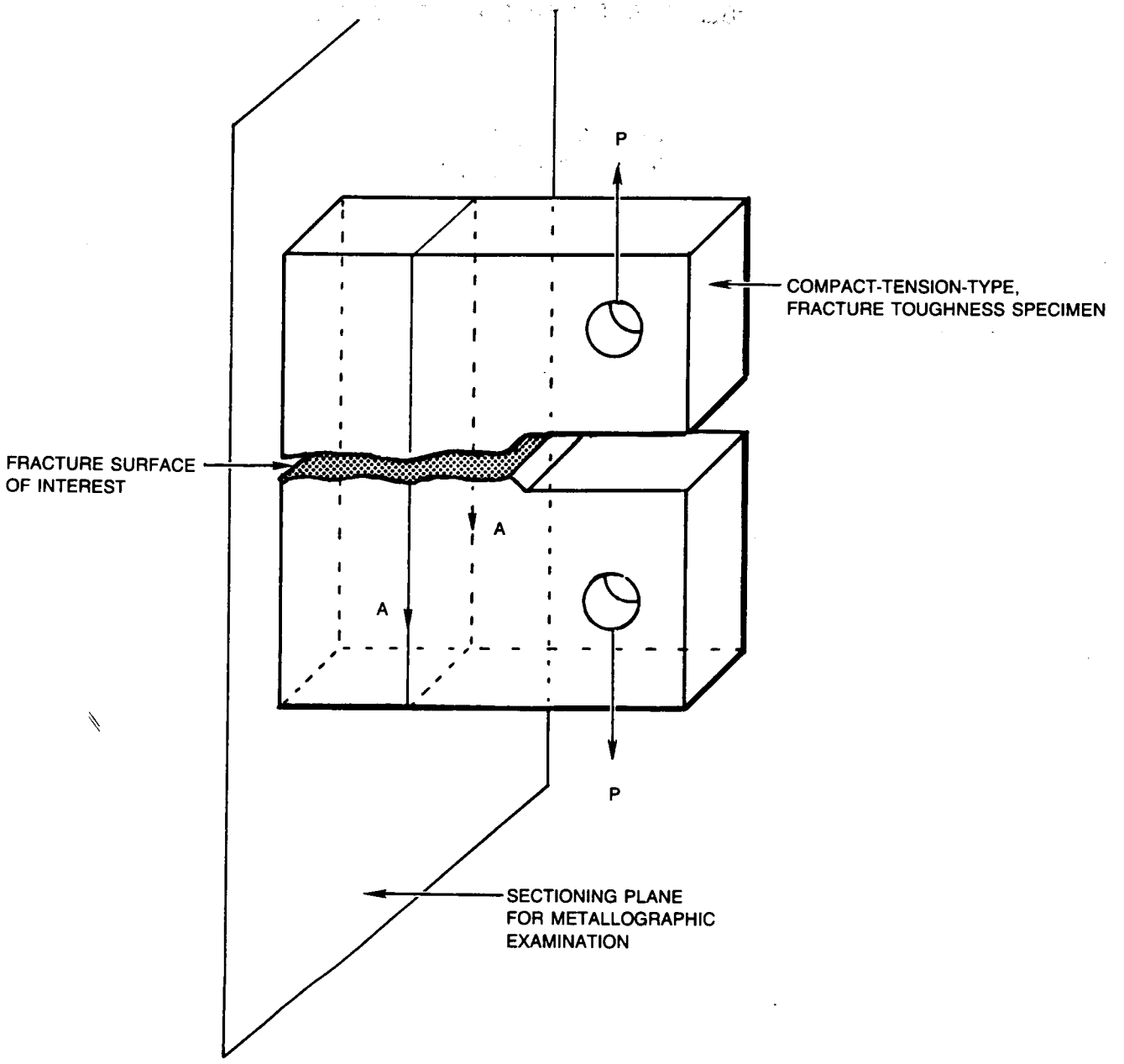

SECTION A-A

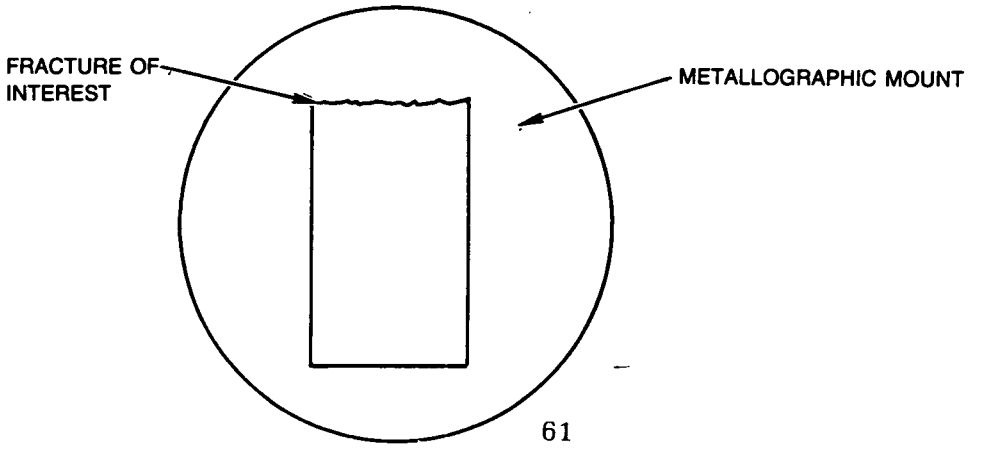

ORIGINAL PAGE
BLACK AND WHITE PHOTOGRAPH

ORIGINAL PAGE IS
OF POOR QUALITY

OPTICAL MICRO-FRACTOGRAPH OF THE LONGITUDINAL (L-T) ORIENTATION FRACTURED AT ROOM TEMPERATURE

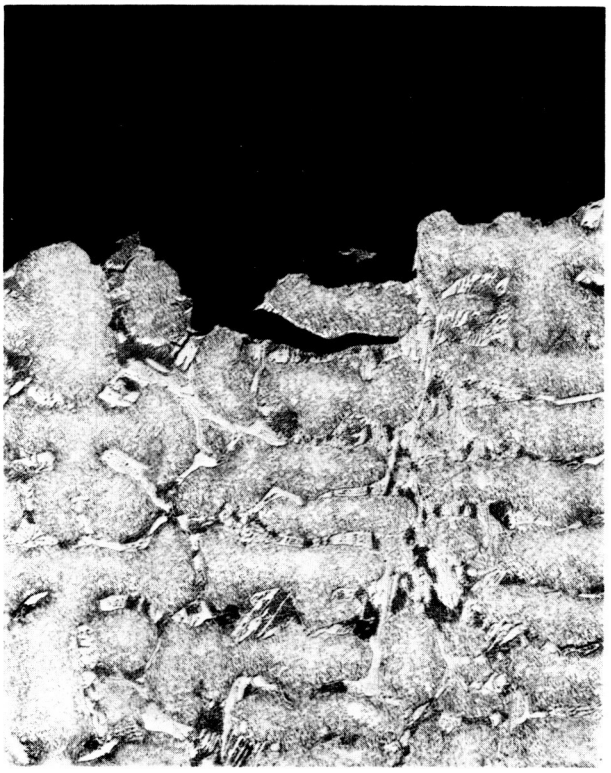

87-10-12-2

FIG. 31

OPTICAL MICRO-FRACTOGRAPH OF THE TRANSVERSE (T-L) ORIENTATION FRACTURED AT ROOM TEMPERATURE

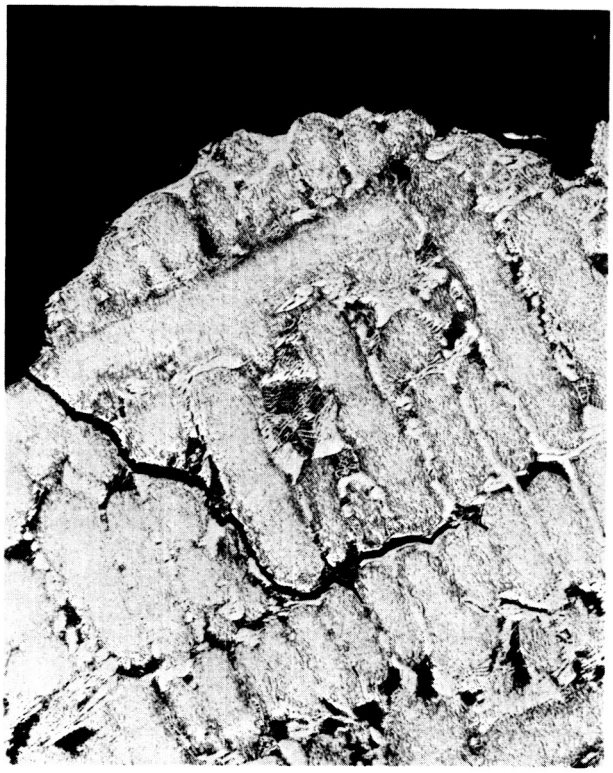

87-10-12-3

FIG. 32

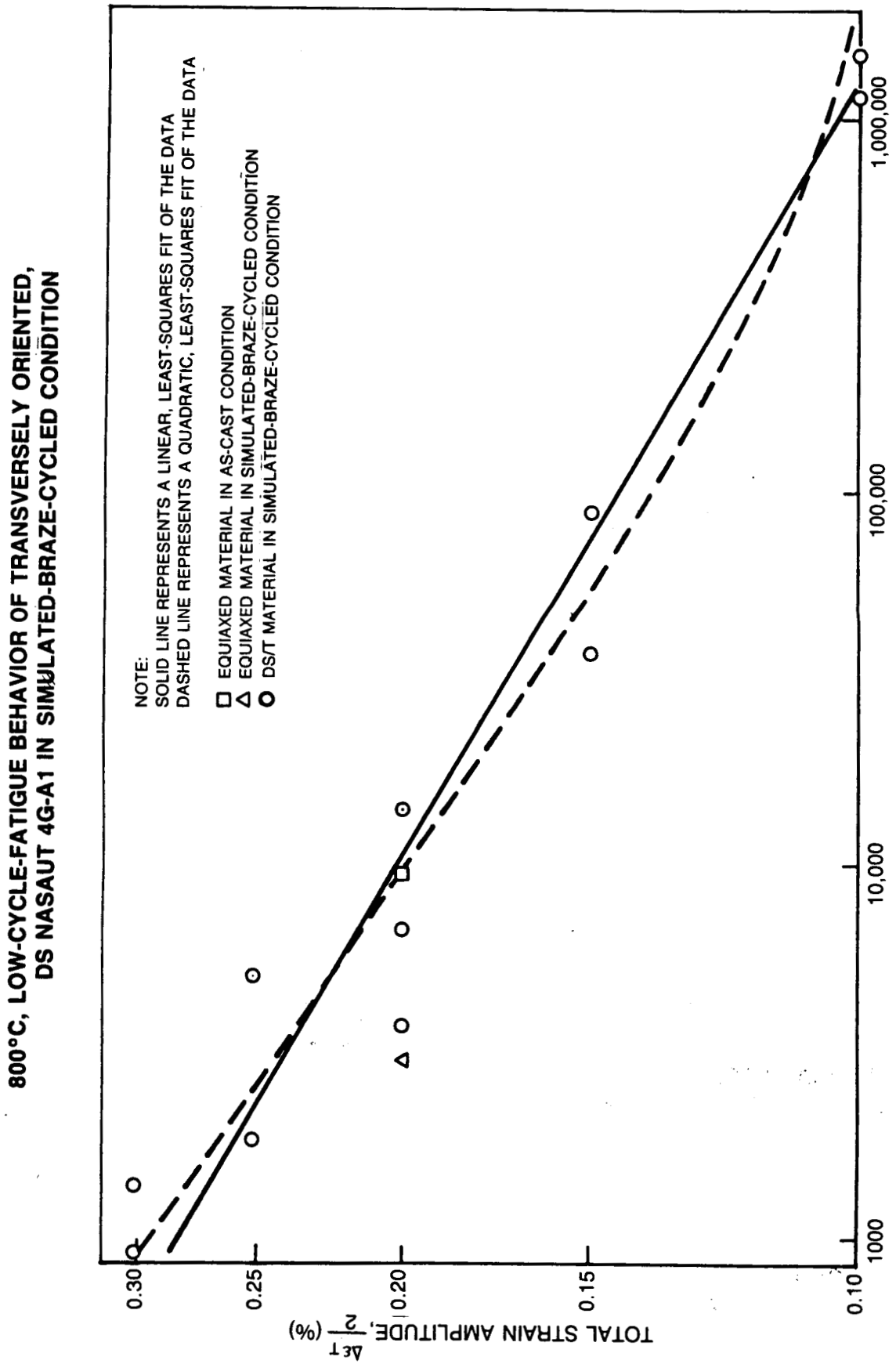

87—12—20—1

HIGH-CYCLE FATIGUE OF VARIOUSLY HEAT-TREATED NASAUT 4G-A1 AT 22°C

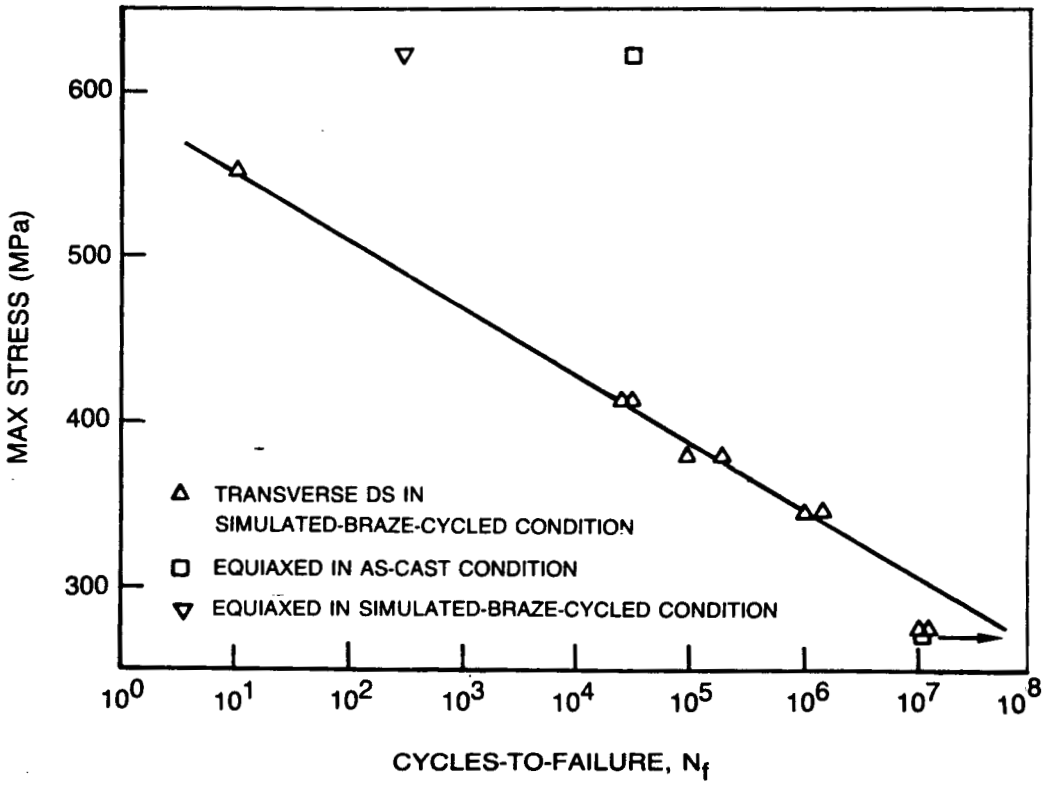

HIGH-CYCLE FATIGUE OF VARIOUSLY HEAT-TREATED NASAUT 4G-A1 AT 200°C

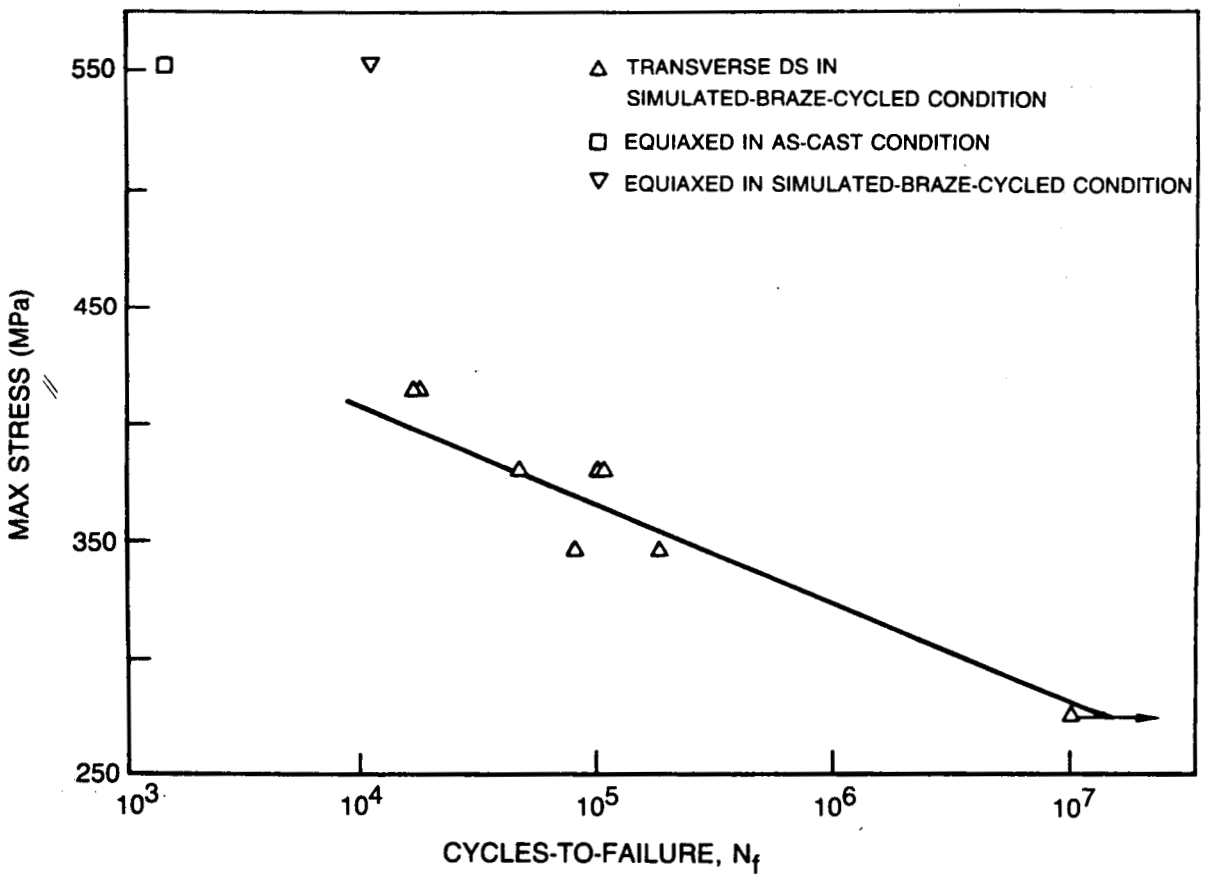

FIG. 35

HIGH-CYCLE FATIGUE OF VARIOUSLY HEAT-TREATED NASAUT 4G-A1 AT 400°C

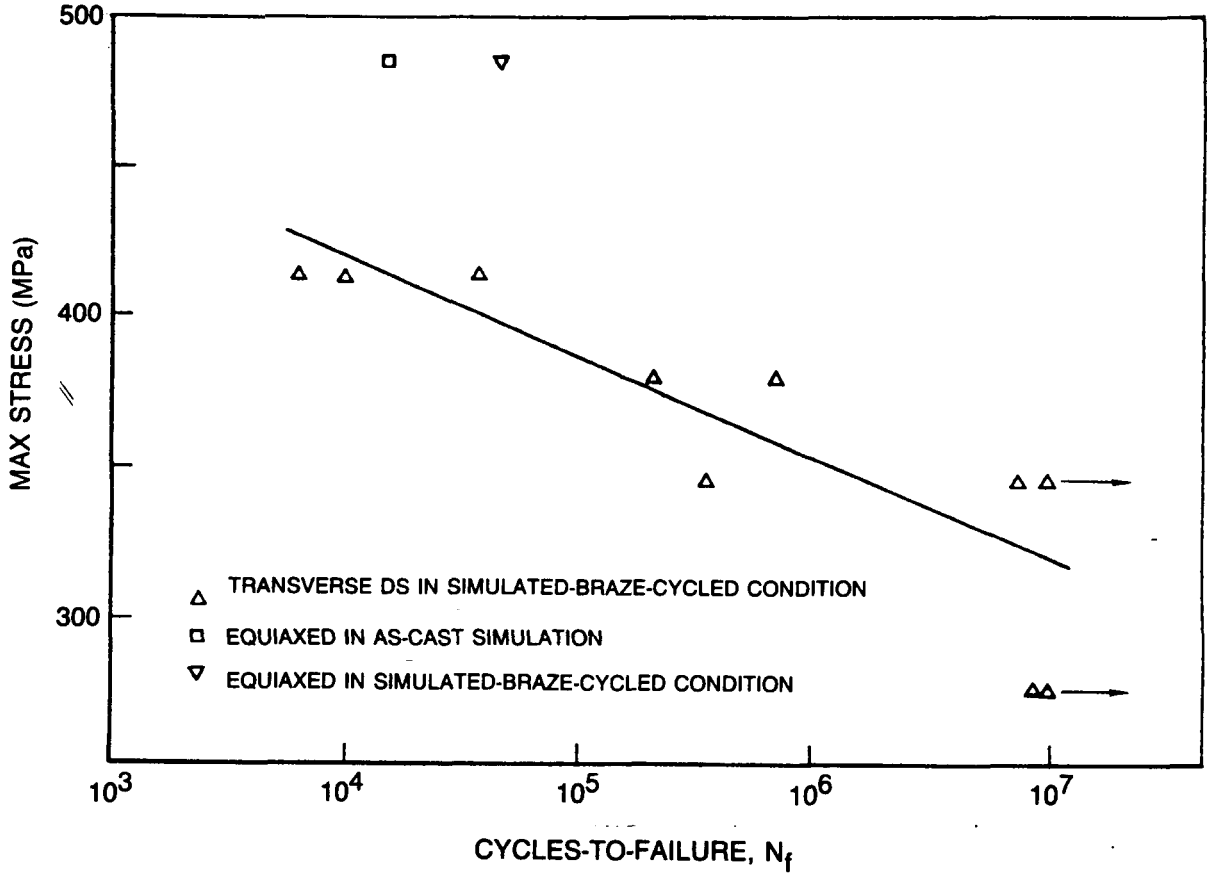

FIG. 36

HIGH-CYCLE FATIGUE OF VARIOUSLY HEAT-TREATED NASAUT 4G-A1 AT 600°C

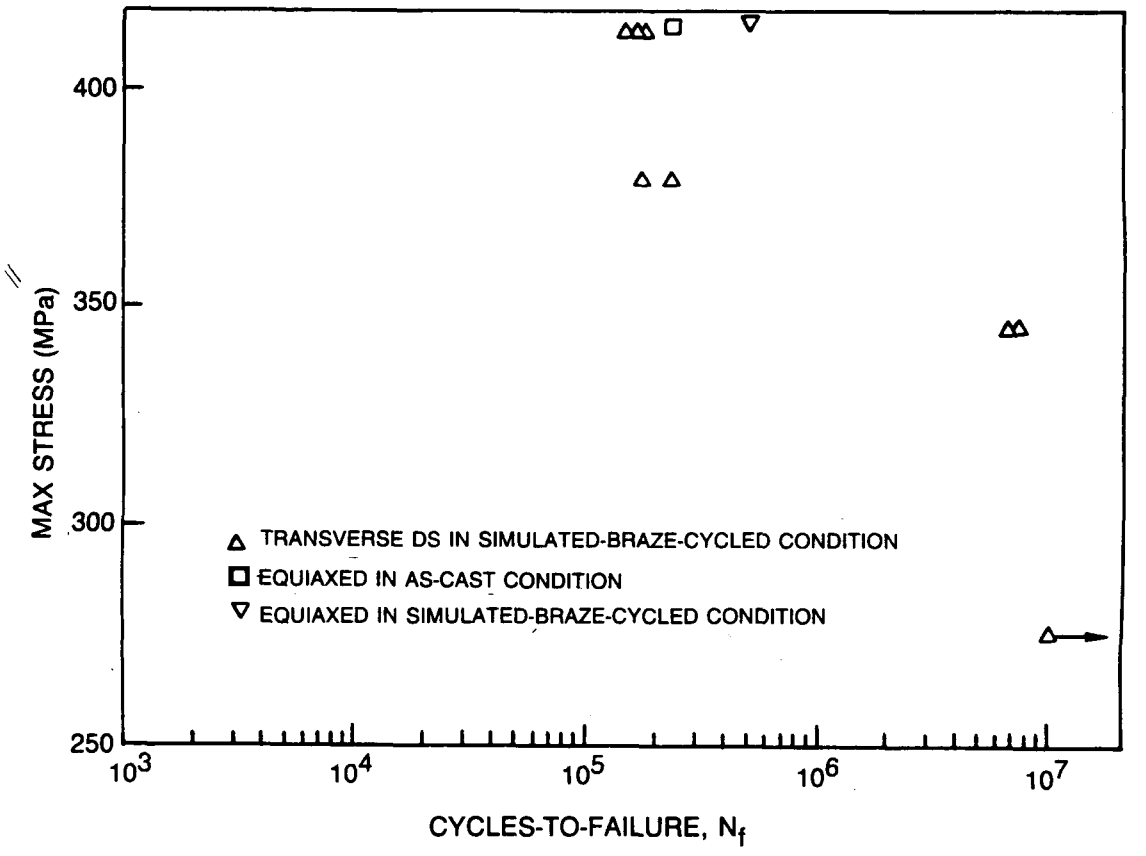

LOW-CYCLE FATIGUE OF SIMULATED-BRAZE-CYCLED, DS/L NASAUT 4G-A1 AT 22°C

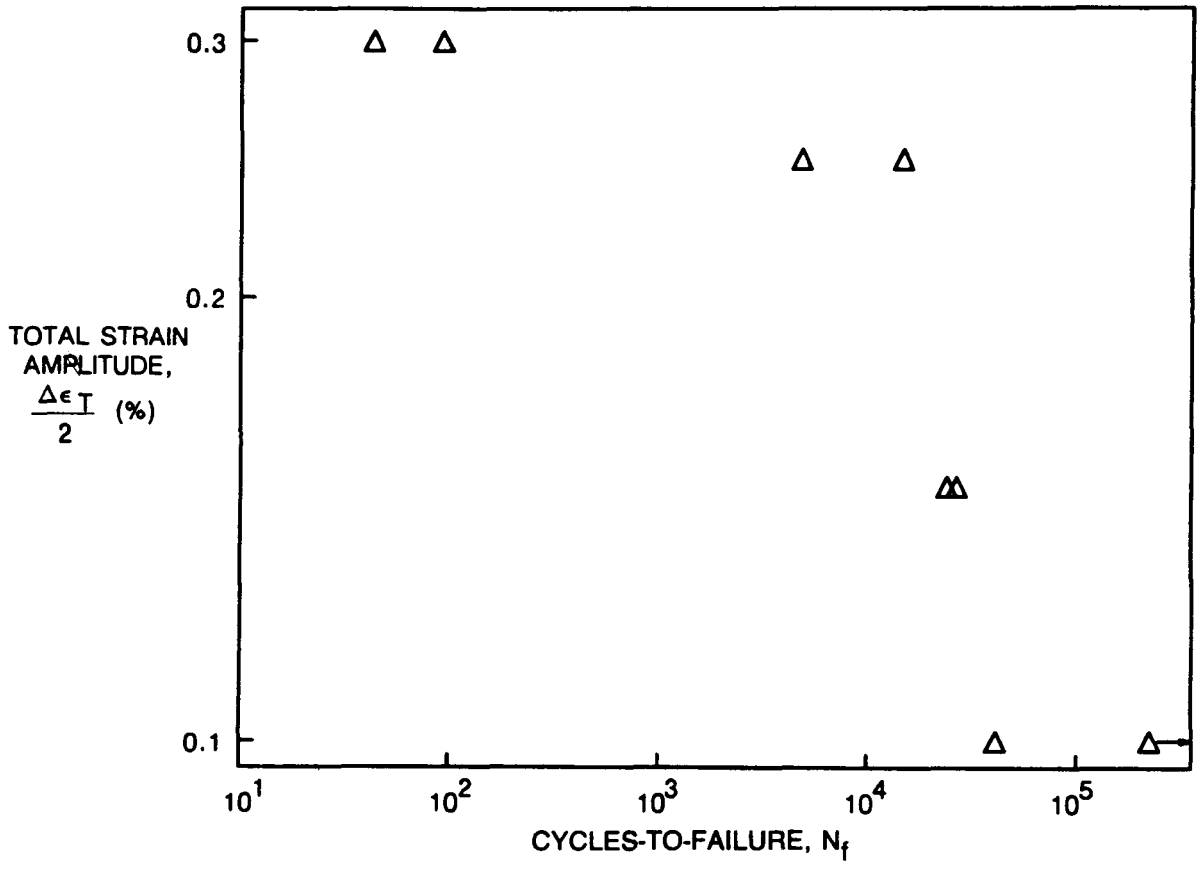

89-3-50-1

FIG. 38

LOW-CYCLE FATIGUE OF SIMULATED-BRAZE-CYCLED, DS/L NASAUT 4G-A1 AT 400°C

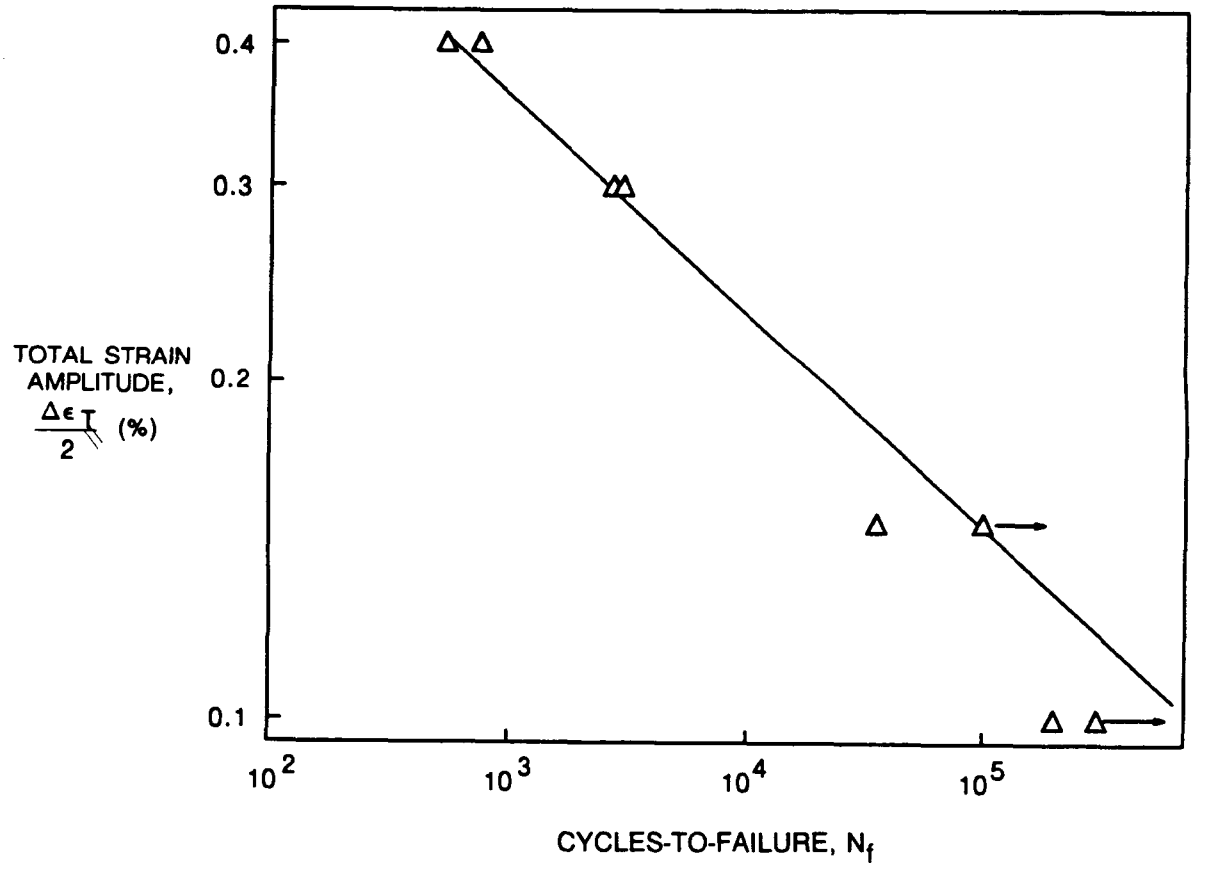

89-3-50-2

FIG. 39

LOW-CYCLE FATIGUE OF SIMULATED-BRAZE-CYCLED, DS/L NASAUT 4G-A1 AT 800°C

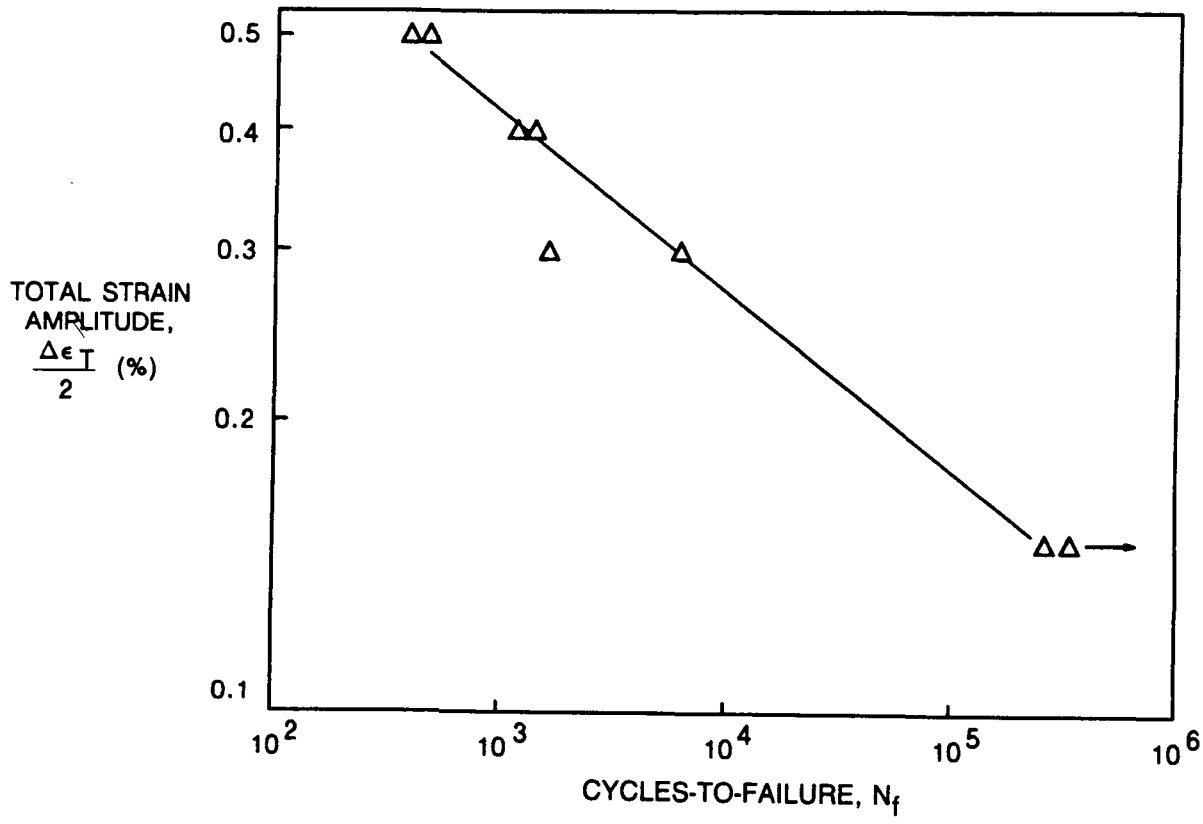

89-3-50-3

FIG. 40

HIGH-CYCLE FATIGUE OF SIMULATED-BRAZE-CYCLED, DS/L NASAUT 4G-A1 AT 22°C

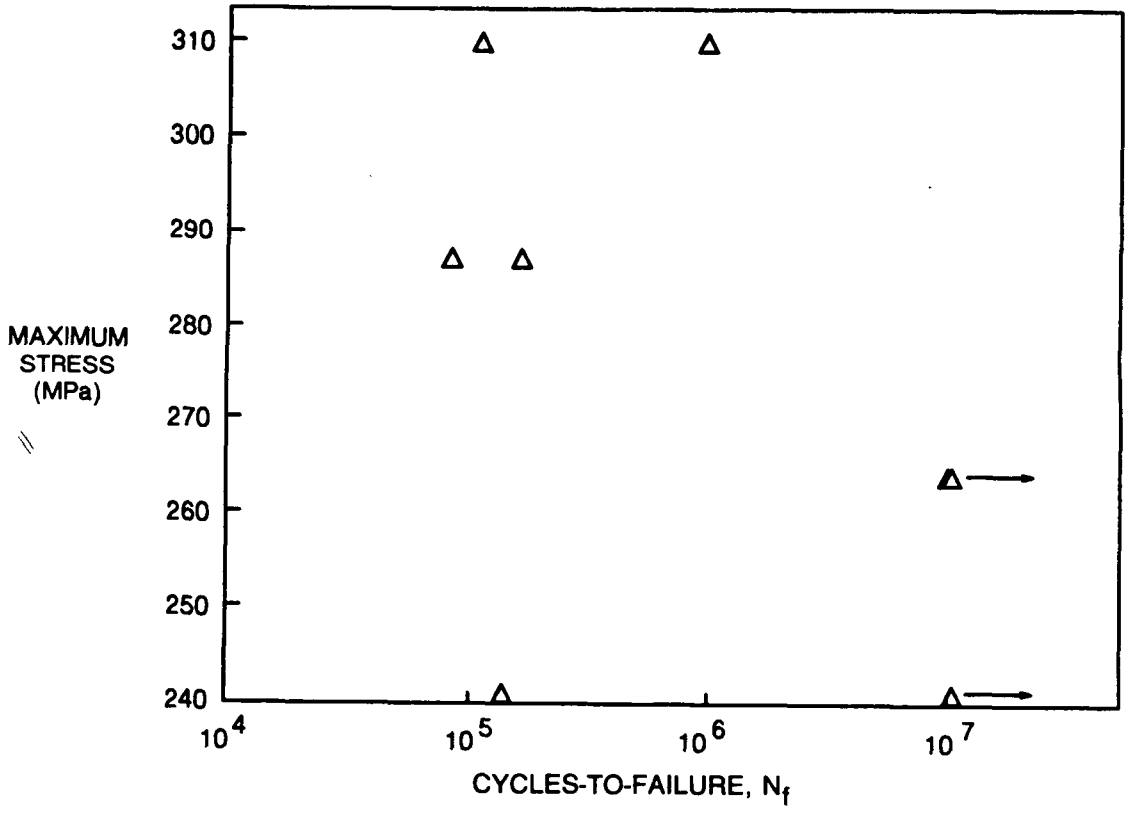

89-3-50-4

HIGH-CYCLE FATIGUE OF SIMULATED-BRAZE-CYCLED, DS/L NASAUT 4G-A1 AT 400°C

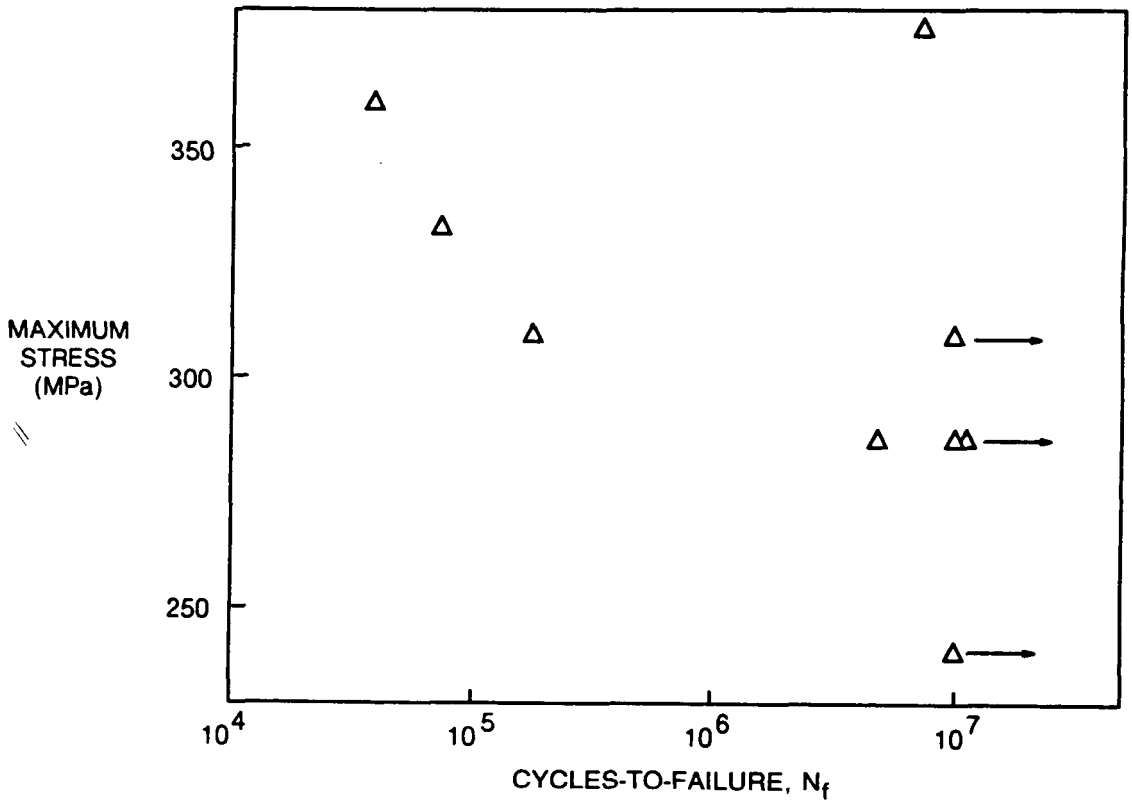

89-3-50-5

HIGH-CYCLE FATIGUE OF SIMULATED-BRAZE-CYCLED, DS/L NASAUT 4G-A1 AT 800°C

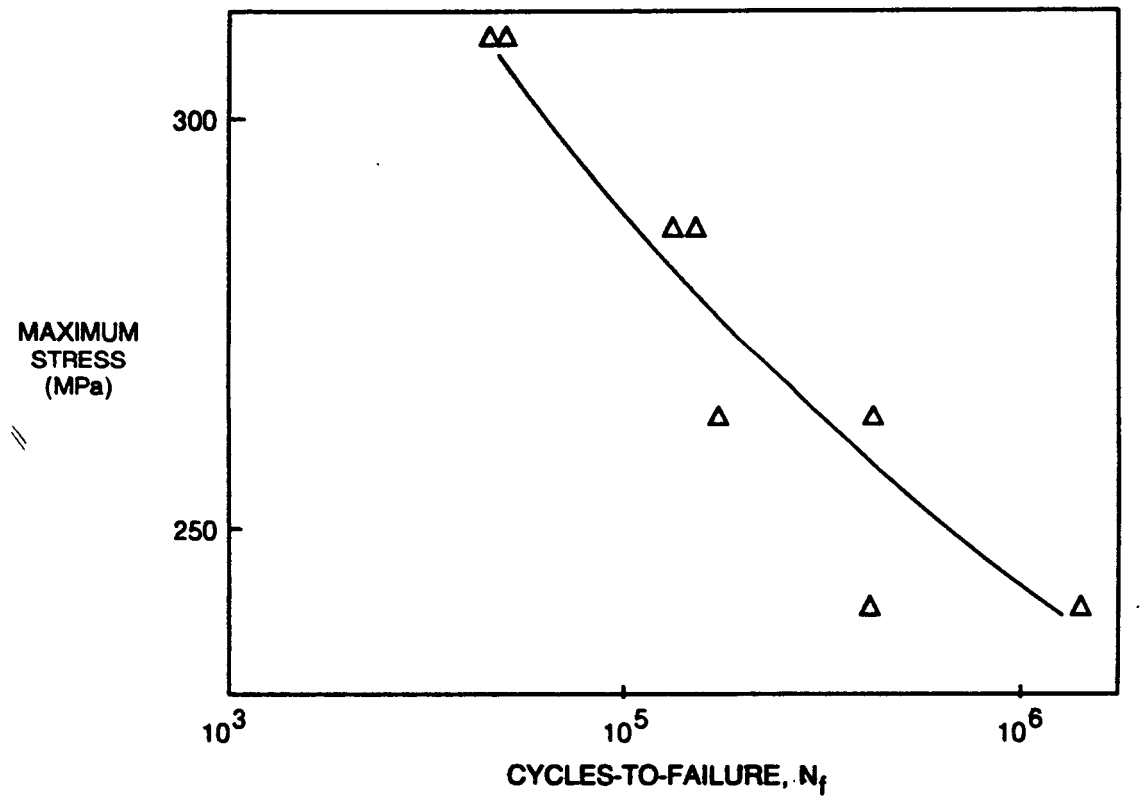

89-3-50-6

NASA
National Aeronautics and Space Administration

Report Documentation Page

1. Report No.	2. Government Accession No.	3. Recipient's Catalog No.
NASA CR-185174 DOE/NASA/0282-1		

4. Title and Subtitle	5. Report Date
Identification of a Cast Iron Alloy Containing Nonstrategic Elements	June 1989
	6. Performing Organization Code

7. Author(s)	8. Performing Organization Report No.
C.V. Cooper, D.L. Anton, F.D. Lemkey, H. Nowotny, R.S. Bailey, L.H. Favrow, J.G. Smeggil, and D.B. Snow	R89-917447-32
	10. Work Unit No.

9. Performing Organization Name and Address	11. Contract or Grant No.
United Technologies Research Center East Hartford, Connecticut 06108	DEN3-282
	13. Type of Report and Period Covered Contractor Report Final

12. Sponsoring Agency Name and Address	14. Sponsoring Agency Code
U.S. Department of Energy Office of Vehicle and Engine R&D Washington, D.C. 20545	

15. Supplementary Notes

Prepared under Interagency Agreement DE-AI01-77CS51040. Project Managers, C.M. Scheuermann and R.H. Titran, Materials Division, NASA Lewis Research Center, Cleveland, Ohio 44135.

16. Abstract

A program has been carried out to address the mechanical and environmental needs of Stirling engine heater head and regenerator housing components, while reducing the dependence on strategic materials. Current candidate materials for such applications contain significant levels of cobalt, nickel, chromium, and/or tantalum. An alloy was developed during this program which contained none of these strategic elemental additions *per se*. The base is iron with additions of manganese, molybdenum, carbon, silicon, niobium, and ferro-chromium. Such an alloy should be producible on a large scale at very low cost. The resulting alloy, designated as NASAUT 4G-A1, contained 15 Mn, 15 Cr, 2 Mo, 1.5 C, 1.0 Si, 1.0 Nb (in weight percent) with a balance of Fe. This alloy (and several others along the development path) was optimized for chemistry, based upon tensile strength, creep-rupture strength, fracture behavior, and fatigue resistance up to 800 °C. Alloys were also tested for environmental compatibility (in air, salt fog, and hydrogen). The microstructure and mechanical properties (including hardness) were assessed in the as-cast condition and following several heat treatments, including one designed to simulate a required braze cycle. The alloy was fabricated and characterized in the form of both equiaxed and columnar-grained castings. The columnar grains were produced by directional solidification, and the properties were characterized in both the longitudinal and transverse orientations. The NASAUT 4G-A1 alloy was found to be good in cyclic-oxidation resistance and excellent in both hydrogen and hot-corrosion resistance, especially in comparison to the baseline XF-818 alloy. The mechanical properties of yield strength, stress-rupture life, high-cycle-fatigue resistance, and low-cycle-fatigue resistance were good to excellent in comparison to the current alloy for this application, HS-31 (X-40), with precise results depending in a complex manner on grain orientation and temperature. If required, the ductility could be improved by lowering the carbon content.

17. Key Words (Suggested by Author(s))	18. Distribution Statement
Automotive Stirling engine; Cast iron alloy; Fatigue; Directional solidification; Nonstrategic elements; NASAUT 4G-A1; Tensile; Creep-rupture	Unclassified – Unlimited Subject Category 26 DOE Category UC-25

19. Security Classif. (of this report)	20. Security Classif. (of this page)	21. No. of pages	22. Price*
Unclassified	Unclassified	78	A05

NASA FORM 1626 OCT 86

*For sale by the National Technical Information Service, Springfield, Virginia 22161

☆U.S. GOVERNMENT PRINTING OFFICE: 1990 - 748-158/00213